Contributions to Mineralogy and Petrology (2024) 179:18
https://doi.org/10.1007/s00410-024-02095-3

ORIGINAL PAPER

Revealing the role of crystal chemistry in REE fractionation in skarn garnets: insights from lattice-strain theory

Guang Wen[1,2] · Jun Qiu[1,2] · Albert H. Hofstra[3] · Daniel E. Harlov[2,4,5] · Zhe Ren[1,2] · Jian-Wei Li[1,2]

Received: 15 September 2023 / Accepted: 31 December 2023 / Published online: 16 February 2024

Abstract

Garnet is a prominent mineral in skarn deposits and its rare earth elements (REE) geochemistry is pivotal for understanding skarn mineralization and fluid evolution. In contrast to magmatic and metamorphic garnets, skarn garnets are mainly grossular-andradite in composition. They exhibit variable REE patterns, spanning from notable heavy (H)-REE enrichment to significant light (L)-REE enrichment, accompanied by negative to positive europium (Eu) anomalies. However, the key factors governing REE fractionation in skarn garnets remain uncertain. This study applies the lattice-strain theory (LST) to investigate the influence of crystal chemistry and structure on REE fractionation in garnets from the Lazhushan Fe skarn deposit in eastern China. Our results demonstrate that the garnet-liquid partition coefficient ratios of D_{La}/D_{Yb} significantly increase (up to 5–7 orders of magnitude) with rising andradite content in garnet. This variation underscores the pivotal role of garnet structure in controlling LREE/HREE fractionation. The results further show that partition coefficient ratios of D_{La}/D_{Sm} are strongly dependent on andradite content in garnets, whereas the D_{Gd}/D_{Yb} ratios only show a weak correlation to the garnet composition. This contrast suggests that fractionation of LREE in garnet is more sensitive to variations of andradite content than HREE. Data compilation of major elements and REE for garnet from the Lazhushan Fe skarn deposit and other skarn deposits worldwide shows that the garnet REE patterns vary from positive through concave to negative shapes with the garnet ranging from grossularitic to andraditic compositions. Such variations in garnet REE patterns are consistent with the results of geochemical modeling based on the LST. This study demonstrates that, through LST equations, the shape of fluid REE patterns can be predicted from garnet REE patterns, and vice versa. Furthermore, the Eu anomaly (Eu/Eu^*_{Grt}) in skarn garnet depends mainly on fluid Eu anomaly (Eu/Eu^*_{fluid}) and garnet-fluid partition coefficient ratio of $D(Eu^{2+})/D(Eu^{3+})$ with the latter being influenced by garnet composition. These findings highlight the critical role of crystal chemistry and structure in garnet REE fractionation, enhancing our ability to utilize garnet REE in tracing the origin and evolution of skarn-forming fluids.

Keywords Garnet · Skarn · REE fractionation · REE pattern · Eu anomaly · Crystal chemistry · Lattice strain theory

Communicated by Dante Canil.

✉ Jian-Wei Li
jwli@cug.edu.cn

[1] State Key Laboratory of Geological Processes and Mineral Resources, China University of Geosciences, Wuhan 430074, China

[2] School of Earth Resources, China University of Geosciences, Wuhan 430074, China

[3] U.S. Geological Survey, P.O. Box 25046, Denver, CO 80225, USA

[4] Deutsches Geoforschungs Zentrum-GFZ, Telegrafenberg, 14473 Potsdam, Germany

[5] Department of Geology, University of Johannesburg, P.O. Box 524, Auckland Park 2006, South Africa

Introduction

Skarn deposits are among the most common ore deposit types in the Earth's crust (Meinert et al. 2005). They are mostly characterized by the abundance of calc-silicate minerals such as garnet and pyroxene that are typically formed via reactions between high temperature fluids and Ca-rich country rocks (Einaudi 1981; Meinert et al. 2005; Chang et al. 2019). It has been shown that garnet from skarns displays large compositional variations and thus can record the physiochemical conditions under which the skarns formed (Jamtveit 1991; Meinert 1992). With the development of modern analytical techniques, such as laser ablation (LA)-ICP-MS that allow fast and accurate analysis at sub ppm

limits, there have been growing interests in using garnet trace elements and, in particular REE, to decipher hydrothermal processes associated with skarn formation. For example, REE in skarn garnets have been used to reflect changes in water/rock ratios (e.g., Gaspar et al. 2008; Xiao et al. 2018) and redox conditions (e.g., Dana et al. 2023), trace fluid origins (e.g., Zhai et al. 2014; Park et al. 2017) and evolutions (e.g., Zhang et al. 2019; Xu et al. 2016; Liu et al. 2021), provide clues on mineral growth mechanisms (e.g., Smith et al. 2004; Gaspar et al. 2008; Park et al. 2017). The general chemical formula of garnet is $X_3Y_2Z_3O_{12}$, where X represents divalent cations (Ca, Mg, Mn, or Fe^{2+}) in eightfold coordination, Y represents trivalent cations (Fe^{3+}, Al, and Cr) in octahedral coordination, and Z is dominantly Si in tetrahedral coordination (Deer et al. 2013). REE are known to be incorporated into garnet by substituting for divalent cations in the eightfold X site, often in coupled substitution with monovalent alkali elements (e.g., van Westrenen et al. 1999; Cahalan et al. 2014; Carlson et al. 2014; Rubatto et al. 2020; Kulhánek and Faryad 2023). REE are generally thought to have order of magnitude slower diffusivities in garnet than the major elements, thus preserving compositional zoning at higher temperatures or for longer durations (e.g., Carlson et al. 2014; Kulhánek et al. 2021). REE zonation within garnet has been shown to provide a wealthy of information to document the changing conditions of garnet growth and modification during metamorphism (e.g., George et al. 2018; Rubatto et al. 2020; Vho et al. 2020; Kulhánek et al. 2021; Goncalves et al. 2021; Aygül et al. 2022; Godet et al. 2022; Konrad-Schmolke et al. 2023; Kulhánek and Faryad 2023). Previous studies have proposed a strong control by crystal structure and chemistry on REE fractionation in magmatic and metamorphic garnets that is characterized by steep patterns of LREE depletion and HREE enrichment with a general negative but variable Eu anomaly (e.g., Irving and Frey 1978; Sisson and Bacon 1992; Harris et al. 1992; Rubatto 2002; Whitehouse and Platt 2003). The Y site in these garnets is dominated by Al, and they mainly consist of pyrope ($Mg_3Al_2Si_3O_{12}$), almandine ($Fe_3Al_2Si_3O_{12}$), spessartine ($Mn_3Al_2Si_3O_{12}$), and grossular ($Ca_3Al_2Si_3O_{12}$) end-members with a minor andradite ($Ca_3Fe_2Si_3O_{12}$) component. In contrast, skarn garnets are mainly andradite-grossular garnets and display highly variable chondrite-normalized REE patterns ranging from notable HREE enrichment to significant LREE enrichment and with negative to positive Eu anomalies (e.g., Smith et al. 2004; Gaspar et al. 2008; Xiao et al. 2018; Park et al. 2017; Fei et al. 2019; Duan et al. 2020; Wang and Duan 2021). To date, however, the extent to which crystal chemistry controls REE fractionation in skarn garnet remains largely unknown. Several factors, including the physicochemical conditions of the garnet-forming fluid (e.g., P, T, pH and compositions; Gaspar et al. 2008; Zhai et al. 2014; Xu et al. 2020), variations of thermodynamic properties (e.g., H_{mixing}) in grossular–andradite (Gaspar et al. 2008; Fei et al. 2019), kinetic effects (Jamtveit and Hervig 1994; Smith et al. 2004; Gaspar et al. 2008), and closed-system fractional crystallization (Smith et al. 2004; Xu et al. 2020) have been proposed to explain the variations in REE patterns and Eu anomalies of skarn garnet. However, the primary controls on REE fractionation in skarn garnets are still uncertain, which limits our ability to employ garnet REE as reliable tracers in skarn systems. Minerals precipitating under equilibrium conditions commonly accommodate trace elements following equilibrium mineral-liquid element partition coefficients (van Hinsberg et al. 2010; 2021). The crystal lattice-strain theory (LST; Blundy and Wood 1994) provides a convenient framework correlating trace element partition coefficients with crystal structure. According to the LST, the partitioning of isovalent cations (e.g., REE^{3+}) can be explained by a simple model based on the size and elasticity of the crystal lattice sites (Blundy and Wood 1994; 2003). Element partition coefficients between a mineral and a liquid vary systematically as a function of the ionic radii of individual elements, which can be described by an expression as follows:

$$D = D_0 \times \exp\left\{\left(-4\pi E_M N_A/\mathrm{RT}\right) \times\left[r_0\left(r_j - r_0\right)^2/2 + \left(r_j - r_0\right)^3/3\right]\right\}, \quad (1)$$

Here, D_0 is the mineral-liquid partition coefficient for strain-free substitution; r_0 is the optimum radius for the lattice site; r_j is the ionic radius of the element of interest; E_M is the effective Young's modulus for the lattice site M;R is the ideal gas constant; N_A is the Avogadro constant; and T is the temperature in K. This relationship is commonly illustrated on an Onuma diagram, plotting the logarithm of the partition coefficient against ionic radius, resulting in a parabolic distribution (Fig. S1). The partition coefficient D_0 for a cation with the optimal radius r_0 determines the "height" of the parabola, while its curvature is determined by the Young's modulus (E_M) for the site. Larger E_M values 'tighten' the parabola, reflecting greater stiffness of the site.

Although the LST has been primarily applied in magmatic systems, recent experimental and empirical investigations have shown that the partitioning of REE between crystals and aqueous fluid follows the LST under equilibrium conditions (Stalder et al. 1998; van Hinsberg et al. 2010; Zhao et al. 2018; Wen et al. 2020). For example, Van Hinsberg et al. (2010) experimentally demonstrated that the partitioning of REE between fluorite and low temperature (60 °C) fluids obeys the LST. Wen et al. (2020) shows that the partitioning of REE between clinopyroxene and the modeled fluid aligns with the LST during skarn formation. In this study, we apply LST to investigate the effect of crystal structure and chemistry on REE fractionation in hydrothermal

garnets from the Lazhushan Fe skarn deposit in eastern China. Our findings, combined with published data from garnets in skarn deposits worldwide, highlight the crucial role of crystal structure and chemistry in REE fractionation in skarn garnets.

Deposit and sample description

The Lazhushan deposit is located in the Daye district, eastern China, with proven reserves of 2.5 Mt Fe at an average grade of 32–52% Fe. It is hosted in Triassic carbonate xenoliths entrained in an Early Cretaceous diorite (Fig. S2). The xenoliths have undergone intense hydrothermal metasomatism presumably related to fluids exsolved from the crystallizing diorite, forming skarn assemblages and associated iron ores (Fig. S2B). Individual ore bodies are columnar or lenticular in morphology. Magnetite is the predominant ore mineral. Minor pyrite, pyrrhotite, and chalcopyrite occur as disseminations replacing the magnetite. Both endoskarn and exoskarn are well developed in the Lazhushan deposit. The endoskarn is characterized by voluminous diopside occurring as a replacement of amphibole, plagioclase, and biotite in the diorite proximal to the carbonate xenoliths. Garnet in the endoskarn mostly occurs as 1 to 5 cm width veins crosscutting the ore-hosting diorite. The exoskarn is massive and consists of diopside and garnet, which is locally overprinted by or replaced with phlogopite, tremolite, serpentine, chlorite, anhydrite, and magnetite. Based on field and paragenetic relations, the formation of the Lazhushan deposit recorded three stages, including prograde, retrograde, and sulfide-anhydrite stages. The prograde stage is mainly represented by garnet and diopside, whereas the retrograde stage is marked by a variety of hydrous minerals such as phlogopite, actinolite, and chlorite, as well as magnetite. The sulfide-anhydrite stage is characterized by the formation of anhydrite and sulfide minerals, including chalcopyrite, pyrrhotite, and pyrite.

Four representative garnet-bearing samples were selected in this study with sample locations and assemblages listed in Table S1. Sample LZS-11a was collected from endoskarn. It is a 1-cm-wide garnet vein that crosscuts the altered diorite (Fig. 1A). The red-brown, subhedral garnets, ranging from 0.5 to 2 mm in size, exhibit intergrowth with plagioclase and partial chlorite replacement (Fig. 2A,B). Homogeneity is generally observed in backscattered electron (BSE) images, with some grains replaced by secondary equivalents at their margins (Fig. 2C). Sample LZS-29 was collected from an exoskarn. It consists of massive garnet aggregates (> 80 vol%) that are cut by an anhydrite vein (Fig. 1B). Anhydrite typically replaces garnets along their grain boundaries (Fig. 2D). The garnets are light brown and subhedral with a grain size of 2 to 3 mm with presence of many fractures (Fig. 2D, E). BSE images reveal two types of garnets based on brightness: Type 1 (T1) is darker than Type 2 (T2), often occurring as irregular domains within T1 garnet (Fig. 2F). Sample LZS-5a was taken from an ore body, which consists of densely disseminated magnetite (60 vol%) with lesser amounts of garnet, pyrite, and calcite (Fig. 1C). The garnets are yellow-green to light brown and euhedral with a grain size of 0.5 to 2 mm (Fig. 2G ,H). Under BSE images, garnets are commonly zoned (Fig. 2I), but homogeneous garnets can also be found. The zoned garnets typically consist a homogeneous core and oscillatory-zoned overgrowth rims (Fig. 2I). Sample LZS-32 was collected from magnetite ore consisting of massive magnetite (> 80 vol%) and minor anhydrite and pyrite (Fig. 1D), with fine-grained garnet (< 500 μm) enclosed in magnetite aggregates. The garnets range in size from 100 to 400 μm and is partly replaced by magnetite, pyrite, and calcite (Fig. 2J, K). Calcite inclusions can be observed in the garnet grains. The garnets are homogeneous under BSE images (Fig. 2L). Garnets from these four samples were analyzed for major and trace element compositions.

Analytical methods

The major element compositions of garnet were measured at Wuhan Sample Solution Analytical Technology, Ltd., Wuhan, China, using a JXA-8230 electron microprobe (EMP) with operating conditions of 15 kV acceleration voltage, 20 nA beam current, and 1 μm beam diameter. Natural silicate minerals were used as standards, including pyrope (Mg, Al, Si), johannsenite (Ca), rutile (Ti), percivalite (Na), K-feldspar (K), chromite (Fe, Cr), and rhodonite (Mn). Spectral lines, peak counting time (seconds), and off-peak background time (seconds) used for the wavelength-dispersive spectroscopy analyses were as follows: K (Kα, 10, 5), Na (Kα, 10, 5), Cr (Kα, 10, 5), Si (Kα, 10, 5), Al (Kα, 10, 5), Mg (Kα, 10, 5), Ca (Kα, 10, 5), Ti (Kα, 10, 5), Mn (Kα, 10, 5), and Fe (Kα, 20, 10). Detection limits for each of the elements are below 0.01 wt%. Each spot analysis was made adjacent to the LA-ICP-MS analysis pit produced during trace element analysis. Wavelength dispersive X-ray (WDX) maps were collected using an accelerating voltage of 20 kV, a beam current of 100 nA, and a counting time of 50 ms/step.

Trace element analysis of garnet was conducted by LA-ICP-MS at Wuhan Sample Solution Analytical Technology Co., Ltd., Wuhan, China. Laser sampling was performed using a GeolasPro laser ablation system that consists of a COMPex-Pro 102 ArF excimer laser (wavelength of 193 nm and maximum energy of 200 mJ) and a MicroLas optical system. An Agilent 7700e quadrupole ICP-MS instrument was used to acquire ion-signal intensities. Helium was used as the carrier gas (0.6 l/min). Argon was used as the make-up gas and mixed with helium via a T-connector before entering the ICP. The

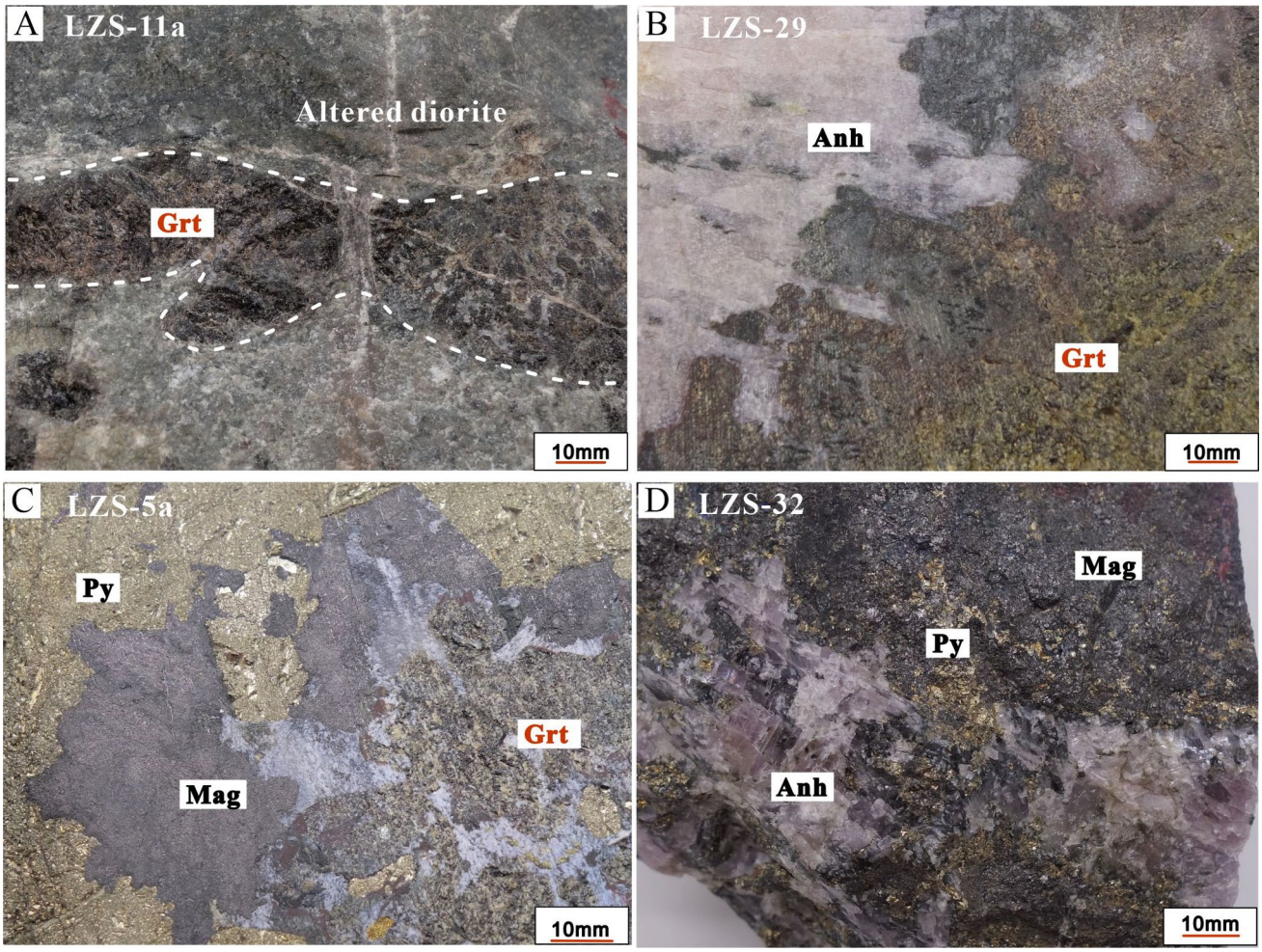

Fig. 1 Photographs showing the four garnet-bearing samples used in this study. **A** Endoskarn garnet vein crosscutting altered diorite. **B** Massive exoskarn garnet overprinted by anhydrite. **C** Garnet coexisting with magnetite, pyrite, and calcite in magnetite ore. **D** Massive magnetite ore sample containing fine-grained garnet (not visible with naked eyes) and disseminated pyrite and anhydrate. Abbreviations: Anh, Anhydrite; Grt, Garnet; Mag, Magnetite; Py, Pyrite; LZS, Lazhushan

laser fluence, spot size, and frequency were 6J/cm^2, 60 μm, and 5 Hz, respectively. National Institute of Standards and Technology (NIST) standard reference material (SRM) 610 was used as the external standard for trace element calibration. The accuracy and precision were monitored by repeated analyses of BCR-2G, BHVO-2G, and BIR-1G standards (Table S2). The preferred values of element concentrations for the NIST SRM 610, BCR-2G, BHVO-2G, and BIR-1G reference glasses are from the GeoReM database (http://georem.mpch-mainz.gwdg.de/). Each analysis involved a background acquisition of approximately 20 to 30 s followed by 50 s of data acquisition from the sample. An Excel-based software, ICPMSDataCal, was used to perform off-line selection and integration of background and analyte signals, time-drift correction, and quantitative calibration for trace element analysis (Liu et al. 2008). Signals were screened visually for heterogeneities such as micro-inclusions or zoning. Trace element concentrations were internally standardized by the Si content of garnet measured using EMP.

Results

Major and trace element compositions of the garnets are listed in Supplementary Tables S3 and S4, respectively. Garnets analyzed consist mainly of andradite-grossular solid solutions, with spessartine, pyrope, almandine and uvarovite collectively less than 5%. Garnets from samples LZS-11a, LZS-29, and LZS-5a exhibit similar compositions, ranging from $Adr_{60}Grs_{39}$ to $Adr_{72}Grs_{27}$, $Adr_{47}Grs_{51}$ to $Adr_{67}Grs_{30}$, and $Adr_{50}Grs_{48}$ to $Adr_{61}Grs_{37}$, respectively (Table S3). In contrast, garnets from sample LZS-32 have substantially higher Fe contents, with compositions of $Adr_{84}Grs_{14}$ to $Adr_{96}Grs_{4}$ (Table S3). Notably, in sample LZS-29, T1

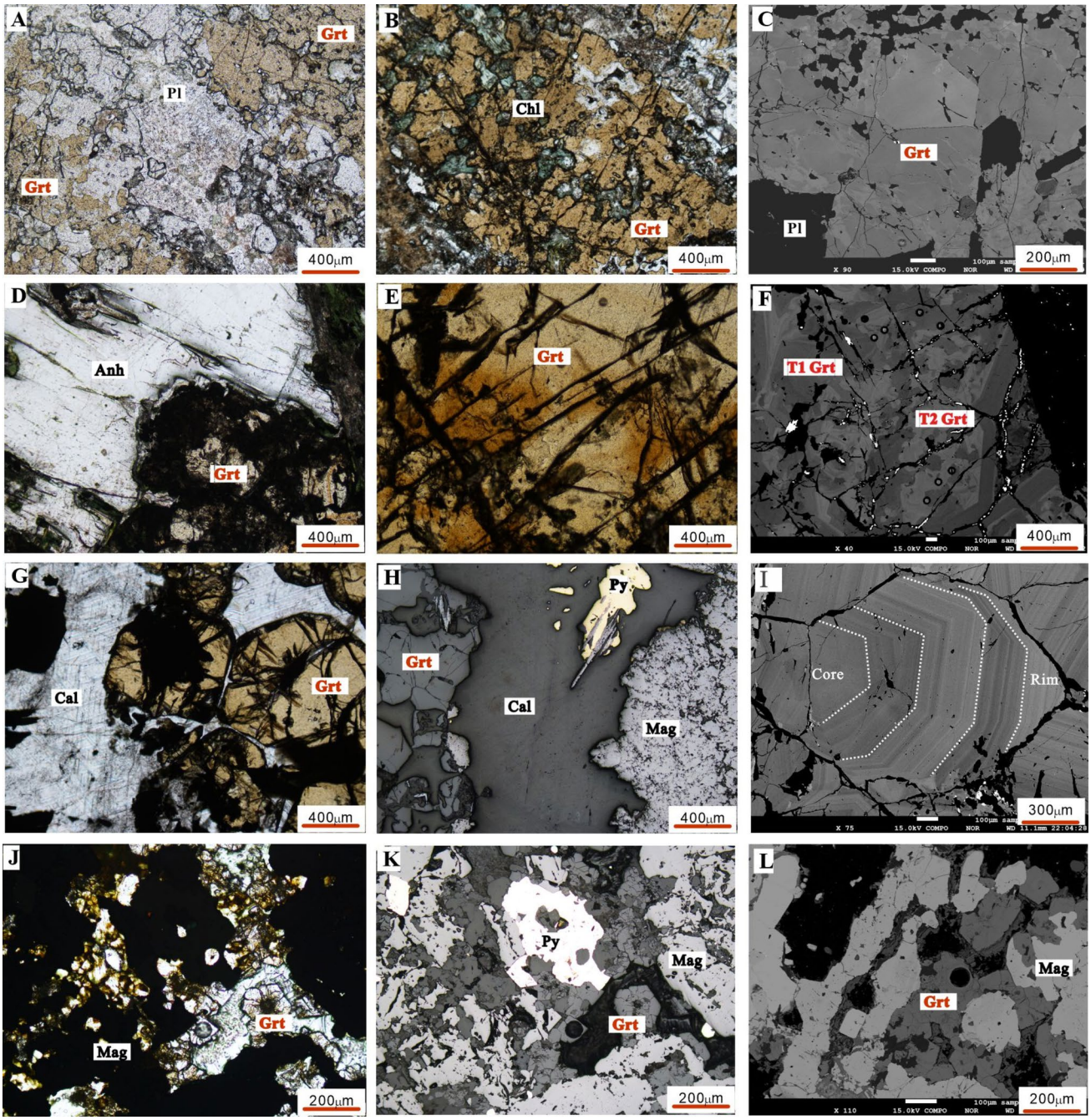

Fig. 2 Photomicrographs and backscattered electron (BSE) images showing garnet textures. Photos of A–C, D–F, G–I and J–L are for garnets from samples of LZS–29, LZS–11a, LZS–5a, and LZS–32, respectively. **A** Subhedral endoskarn garnet intergrows with plagioclase in the altered diorite. **B** Endoskarn garnet locally replaced by chlorite. **C** Some endoskarn garnets replaced by a secondary equivalent at grain margins. **D–E** Subhedral garnet from exoskarn locally replaced by anhydrate. **F** T2 garnet (brighter under BSE) occurring as irregular domains within T1 garnet. **G–H** Garnet coexisting with magnetite, pyrite, and calcite in magnetite ore. **I** The zoned garnet consisting a homogeneous core and oscillatory-zoned overgrowth rims under BSE imaging. **J–K** Fine-grained garnet coexisting with magnetite and pyrite. **L** Homogenous garnet under BSE image. Mineral abbreviations: Anh, Anhydrite; Grt, Garnet; Mag, Magnetite; Py, Pyrite; Cal, Calcite; Chl, Chlorite; Pl, Plagioclase

garnet (Adr_{47-51}) displays lower Fe contents than T2 garnet (Adr_{58-66}). X-ray mapping reveals that the zoned garnet from sample LZS-5a typically features a relatively Fe-rich core (Adr_{55}) and several overgrowth rims (Adr_{50-54}) with rhythmic variations in Fe, Al and Mg concentrations, while Ca contents remain relatively constant throughout the grain (Fig. 3).

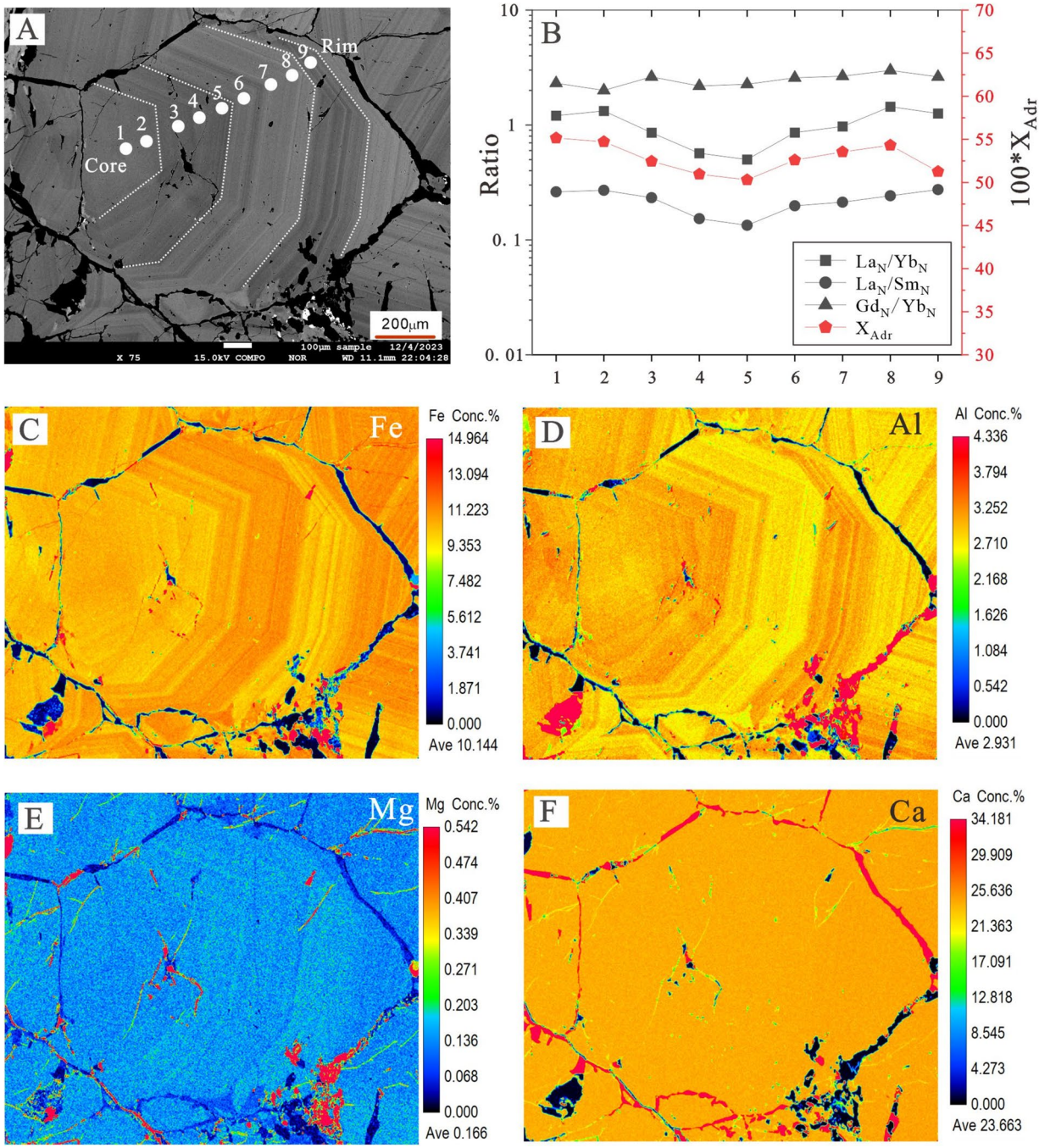

Fig. 3 Backscattered electron image of the zoned garnet with positions of the analysis marked (**A**). Major and trace element profile of the zoned garnet showing core-rim variations of andradite contents and ratios of La_N/Yb_N, La_N/Sm_N and Gd_N/Yb_N (**B**); Compositional maps of Fe (**C**), Al (**D**), Mg (**E**) and Ca (**F**) for the zoned garnet measured by wavelength dispersive X-ray (WDS) on electron microprobe

Among the samples, garnets from LZS-11a exhibit the highest REE contents (∑REE = 209.0–489.1 ppm). In sample LZS-29, T1 garnet is more enriched in REE (∑REE = 216.5–344.9 ppm) than T2 equivalent (∑REE = 99.3–167.9 ppm). Garnets from LZS-5a show total REE concentrations ranging from 158.4 to 301.0 ppm, with the zoned garnets having relatively REE-depleted cores (∑REE = 188.6–199.8 ppm) and REE-enriched rims (∑REE = 171.6–301.0 ppm). In comparison with garnets from the other samples, LZS-5a garnets exhibit a wider range of REE contents (∑REE = 63.5–474.2 ppm). Chondrite-normalized REE diagrams (McDonough and Sun 1995) reveal broadly comparable HREE patterns characterized by flat to slightly negative slopes for garnets from

all four samples. However, the LREE patterns vary significantly among the different samples. Garnets from samples LZS-11a, LZS-29, and LZS-5a display steep positive slopes (Fig. 4A–C). In contrast, those in sample LZS-32 have moderate negative slopes (Fig. 4D). In addition, garnets from sample LZS-32 display negative but variable Eu anomalies, which are not observed in garnets from the other samples (Fig. 4). For all samples, the garnet shows strong positive correlations between La_N/Yb_N or La_N/Sm_N ratios and the andradite contents, with Gd_N/Yb_N ratios being relatively constant (Fig. 5 A–C). The major and trace element profile for the zoned garnet from LZS-5a illustrates coherent variations in andradite contents and La_N/Yb_N and La_N/Sm_N ratios from the core to the rim, while Gd_N/Yb_N ratios remain relatively constant (Fig. 3B). Overall, the garnet REE patterns do not show much variation with regard to sample location or mineral assemblages (endoskarn vs. exoskarn vs. magnetite ore; Figs. 1, 4), but vary significantly with respect to their garnet major element compositions (i.e., andradite contents; Figs. 4, 5).

Discussion

REE fractionation in garnet

The strong positive correlation observed between La_N/Yb_N ratios and andradite contents in the Lazhushan garnet (Fig. 5A) indicates that the degree of LREE/HREE fractionation in garnet is predominantly linked to its major element compositions. Sush a correlation has been observed for garnets from various skarn deposits (e.g., Gaspar et al. 2008; Xiao et al. 2018; Fei et al. 2019; Wang and Duan 2021). To quantitatively elucidate the relationship between garnet

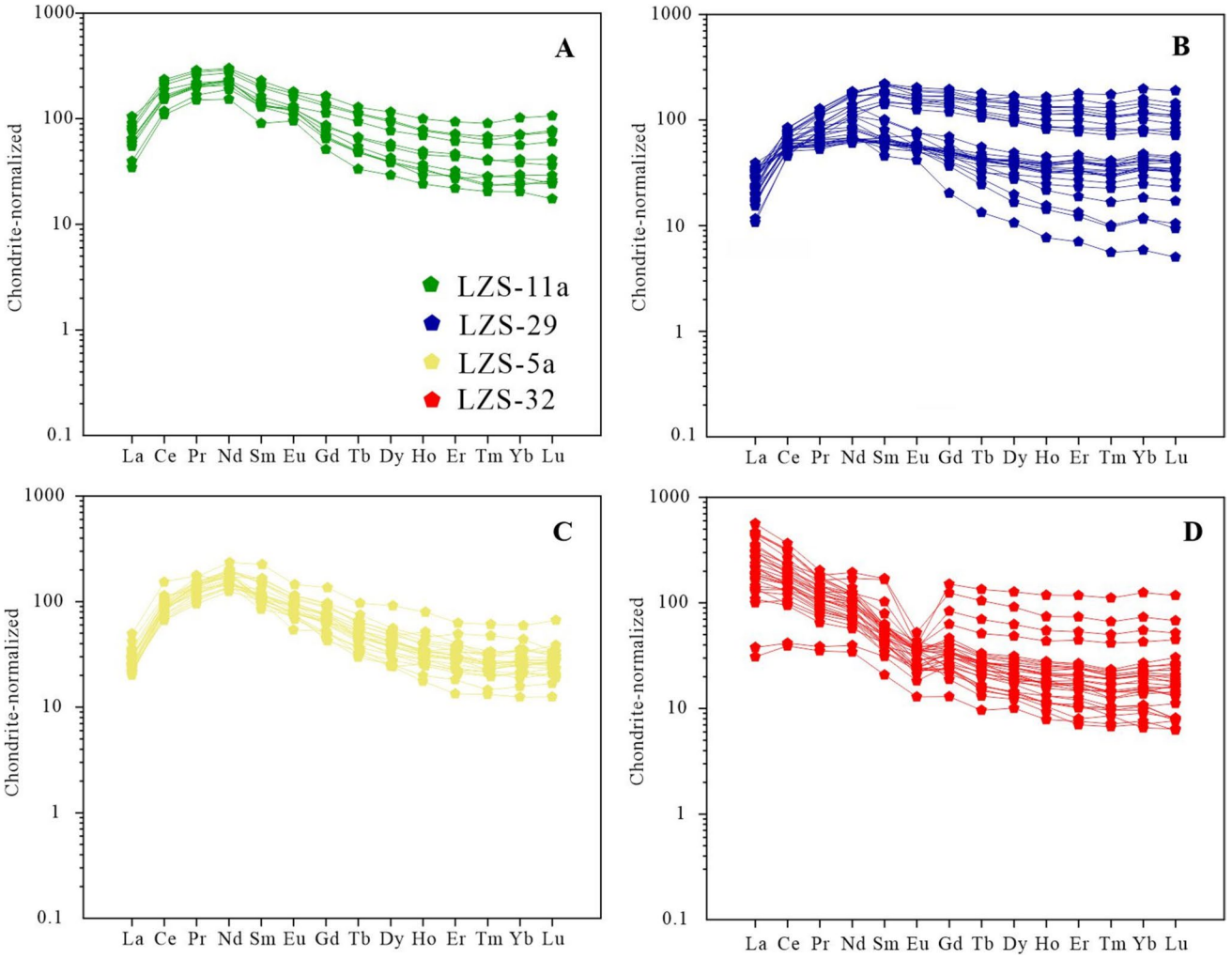

Fig. 4 Chondrite-normalized rare earth elements (REE) patterns of the garnets from samples LZS-11a (**A**), LZS-29 (**B**), LZS-5a (**C**) and LZS-32 (**D**). Garnets from samples LZS–11rare earth elementsa, LZS–29, and LZS-5a display concave shapes (positive slopes of LREE and negative slopes of HREE; A–C), whereas gannets from sample LZS-32 show negative shapes in chondrite-normalized REE diagrams (**D**)

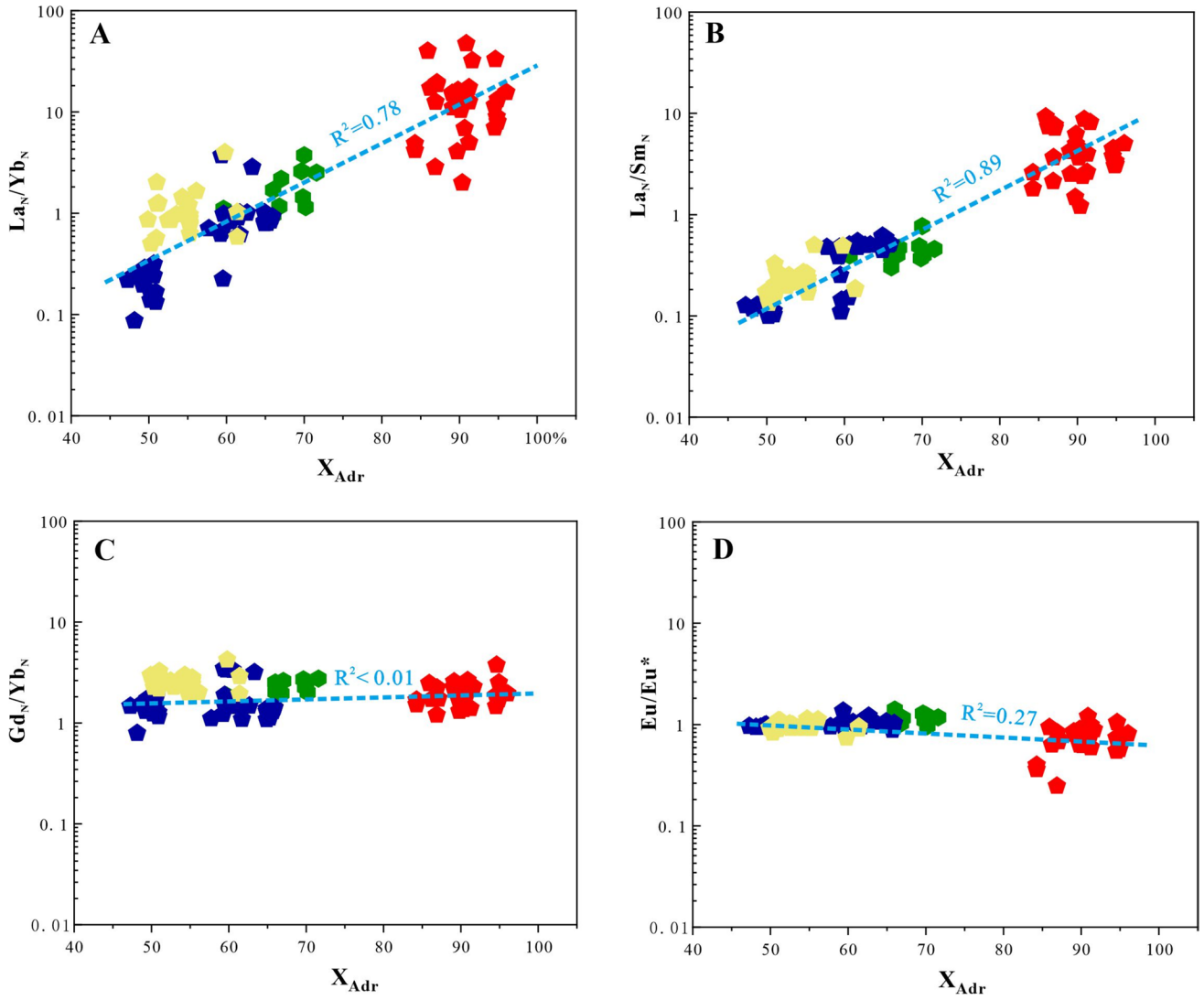

Fig. 5 Mole fraction of andradite (X_{Adr}) vs. La_N/Yb_N (**A**), La_N/Sm_N (**B**), Gd_N/Yb_N (**C**) and Eu/Eu^* (**D**) plots for garnets from the Lazhushan Fe skarn deposit. $Eu/Eu^* = Eu_N/\text{sqrt}(Sm_N \times Gd_N)$. Here "*N*" denotes chondrite-normalized values

chemistry and REE distribution, we apply the LST of Brice (1975) and Blundy and Wood (1994), which has been effectively utilized for quantifying element partitioning between minerals and melts or fluids (Blundy and Wood 2003; van Hinsberg et al. 2010).

Based on LST equation (Eq. 1), the partition coefficient ratios of two specific trivalent REE (D_{REEj}/D_{REEi}, where REEj and REEi are the two different REE elements of interest) can be given by:

$$D_{REEj}/D_{REEi} = \exp\left\{\left(-4\pi E_{M(3+)}N_A/RT\right) \times\left[r_{0(3+)}\left(r^2_{REEi} - r^2_{REEj}\right)/2 - \left(r^3_{REEi} - r^3_{REEj}\right)/3\right]\right\}, \quad (2)$$

As illustrated by Eq. 2, the partition coefficient ratios of D_{REEj}/D_{REEi} are dependent on the LST parameters of $r_{0(3+)}$ and $E_{M(3+)}$ but are independent of $D_{0(3+)}$. To calculate $r_{0(3+)}$ and $E_{M(3+)}$, we assume that the equations from van Westrenen and Draper (2007), originally calibrated for magmatic garnet, can be applied to hydrothermal garnet. This assumption is based on the consideration that $r_{0(3+)}$ and $E_{M(3+)}$ are dominantly controlled by the crystal chemistry rather than other factors, such as the melt/fluid compositions (Blundy and Wood 1994; van Hinsberg et al. 2010). According to van Westrenen and Draper (2007), $r_{0(3+)}$ and $E_{M(3+)}$ can be estimated using the following expressions:

$$r_{0(3+)}\left(\text{Å}\right) = 0.9302X_{Prp} + 0.993X_{Grs} + 0.916X_{Alm} + 0.946\,X_{Sps} + 1.05\left(X_{Adr} + X_{Uv}\right) - 0.0044(\pm 0.0003) \times (P-3) + 0.000058(\pm 0.000007) \times (T - 1818), \quad (3)$$

and.

$$E_{(M3+)}(\mathrm{GPa}) = 2826(\pm174)\times\left(1.38+r_0\right)^{-3} + 12.4(\pm1.3)\times P - 0.072(\pm0.007)\times T + 237(\pm8)\times(\mathrm{Al}+\mathrm{Cr})_{\mathrm{apfu}}, \quad (4)$$

where P is pressure in GPa, T is temperature in K, $(\mathrm{Al}+\mathrm{Cr})_{\mathrm{apfu}}$ denotes the number of atoms per formula unit (12 oxygens) of Al and Cr in garnet, and X refers to the mole fraction.

We use the $D_{\mathrm{La}}/D_{\mathrm{Yb}}$ ratio as an index for the effect of the crystal chemistry on garnet LREE/HREE fractionation. For pure grossular-andradite solid solutions relevant to skarn garnet, X_{Py}, X_{Alm}, X_{Sps}, and X_{Uv} can be considered approximately 0, whereas X_{Grs} and $(\mathrm{Al}+\mathrm{Cr})_{\mathrm{apfu}}$ approximate to 1-X_{Adr} and 2(1–X_{Adr}), respectively. Using the eightfold effective ionic radius of La^{3+} and Yb^{3+} from Shannon (1976), the $D_{\mathrm{La}}/D_{\mathrm{Yb}}$ ratio is calculated by the following equation:

$$D_{La}/D_{Yb} = \exp\left\{\left(-4\pi E_{M(3+)}N_A/\mathrm{RT}\right)\times\left[r_{0(3+)}\times\left(0.985^2-1.16^2\right)\times10^{-20}/2-\left(0.985^3-1.16^3\right)\times10^{-30}/3\right]\right\}, \quad (5)$$

where $r_{0(3+)}$ and $E_{\mathrm{M}(3+)}$ are calculated by:

$$r_{0(3+)}\begin{pmatrix}0\\A\end{pmatrix} = 0.993\times\left(1-X_{\mathrm{Adr}}\right)+1.05\times X_{\mathrm{Adr}} - 0.0044\times(P-3)+0.000058\times(T-1818), \quad (6)$$

$$E_{M(3+)}(\mathrm{GPa}) = 2826\times\left[1.38+0.993\times\left(1-X_{\mathrm{Adr}}\right)+1.05\times X_{\mathrm{Adr}} -0.0044\times(P-3)+0.000058\times(T-1818)\right]^{-3} + 12.4\times P-0.072\times T+237\times2\times\left(1-X_{\mathrm{Adr}}\right), \quad (7)$$

According to Eqs. 5,and 6, and 7, the $D_{\mathrm{La}}/D_{\mathrm{Yb}}$ ratio is a function of temperature, pressure, and the andradite contents of garnet. Therefore, under certain P–T conditions, the $D_{\mathrm{La}}/D_{\mathrm{Yb}}$ ratio depends solely on X_{Adr}. Given a reasonable P–T range of 0.1 to 0.5 GPa and 400 to 600 °C for skarn garnet formation (Meinert et al. 2005), we are able to establish relationships between $D_{\mathrm{La}}/D_{\mathrm{Yb}}$ and X_{Adr}, which are illustrated in Fig. 6. It is obvious that a pressure variation from 0.1 to 0.5 GPa has virtually no effect on $D_{\mathrm{La}}/D_{\mathrm{Yb}}$ while a variation in the temperature from 400 to 600 °C shows some effect (less than 3 orders of magnitude difference; Fig. 6). Instead, the $D_{\mathrm{La}}/D_{\mathrm{Yb}}$ ratio increases dramatically (up to five to seven orders of magnitude difference) with increasing andradite content (Fig. 6). The modeling results demonstrate the prominent role of garnet composition on LREE/HREE fractionation. This finding explains the strong correlation between the La_N/Yb_N ratios and X_{Adr} contents observed for garnets from the Lazhushan iron skarn deposit (Fig. 5A). The La_N/Yb_N ratio of garnet is positively correlated with $D_{\mathrm{La}}/D_{\mathrm{Yb}}$ as illustrated by Eq. 8:

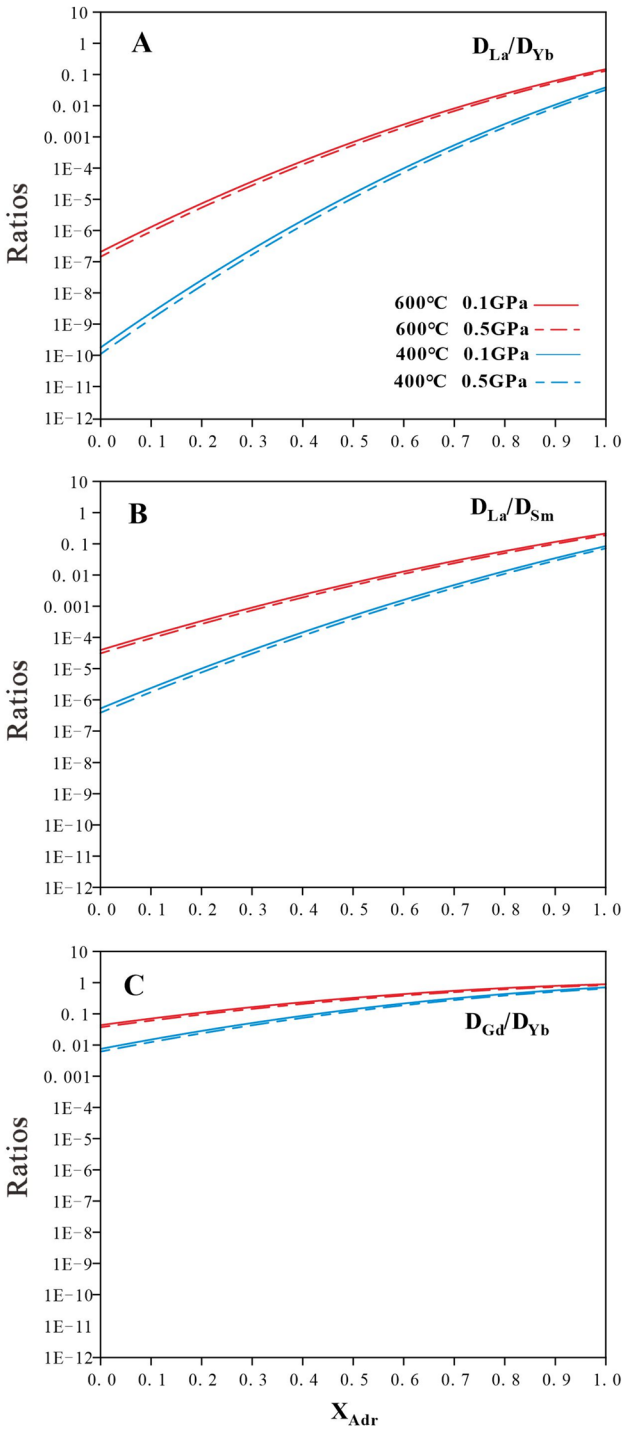

Fig. 6 Correlations between X_{Adr} and garnet-fluid partition coefficient ratios of $D_{\mathrm{La}}/D_{\mathrm{Yb}}$ (**A**), $D_{\mathrm{La}}/D_{\mathrm{Sm}}$ (**B**), and $D_{\mathrm{Gd}}/D_{\mathrm{Yb}}$ (**C**) based on the modeling using LST. Given that REE reside exclusively in the dodecahedral X site in garnet structure (van Westrenen et al. 1999 and references therein), the eightfold effective ionic radius of REE^{3+} (from Shannon 1976) were used for the LST equations

$$(La_N/Yb_N)_{Grt} = D_{La}/D_{Yb} \times (La_N/Yb_N)_{fluid}, \quad (8)$$

where $(La_N/Yb_N)_{Grt}$ and $(La_N/Yb_N)_{fluid}$ are the La_N/Yb_N ratios of the garnet and fluid, respectively.

The partition coefficient ratios for D_{La}/D_{Sm} and D_{Gd}/D_{Yb} are used as indices for charting the effect of crystal chemistry on the fractionation of garnet LREE and HREE, respectively. The D_{La}/D_{Sm} and D_{Gd}/D_{Yb} ratios can be correlated with the andradite content in a manner similar to that for D_{La}/D_{Yb} via the equations:

$$D_{La}/D_{Sm} = \exp\{(-4\pi E_{M(3+)}N_A/RT) \times [r_{0(3+)} \times (1.079^2 - 1.16^2) \times 10^{-20}/2 - (1.079^3 - 1.16^3) \times 10^{-30}/3]\}, \quad (9)$$

$$D_{Gd}/D_{Yb} = \exp\{(-4\pi E_{M(3+)}N_A/RT) \times [r_{0(3+)} \times (0.985^2 - 1.053^2) \times 10^{-20}/2 - (0.985^3 - 1.053^3) \times 10^{-30}/3]\}, \quad (10)$$

where $r_{0(3+)}$ and $E_{M(3+)}$ are calculated by Eqs. 6 and 7, respectively. These correlations reveal a significant dependence on the D_{La}/D_{Sm} ratios and a weak dependence on the D_{Gd}/D_{Yb} ratios with respect to X_{Adr} (Fig. 6), indicating that LREE is more sensitive to the change of garnet major element composition. It is worth noting that some skarn garnets, predominantly found in W and Sn skarns, can contain appreciable amounts of pyrope ($Mg_3Al_2Si_3O_{12}$), almandine ($Fe_3Al_2Si_3O_{12}$) and spessartine ($Mn_3Al_2Si_3O_{12}$) (Meinert 1992). Incorporating these components into calcic garnet enhances the stiffness of the garnet lattice site (i.e., increasing $E_{M(3+)}$; Eqs. 3 and 4), leading to steeper correlations than those depicted in Fig. 6.

Compilation of geochemical analyses ($n = 1127$) of garnet from 22 skarn deposits worldwide provides supporting evidence for the key controls of garnet composition on REE fractionation (Fig. 7; Table S5). Most of the garnets from the dataset are grossular-andradite in composition, with 1098 analyses showing $X_{Adr} + X_{Grs} > 0.9$ (Table S5). It is evident that the garnet La_N/Yb_N ratios from all these skarn deposits are overall strongly correlated with the X_{Adr}, with rare exceptions where low X_{Adr} may display high La_N/Yb_N ratios (Fig. 7 A). This observation suggests that, as a first approximation, LREE/HREE fractionation in skarn garnet is primarily controlled by the major element compositions (i.e., X_{Adr}), despite variations in P, T, fluid composition, and kinetic effects associated with garnet precipitation among those deposits. The apparent positive correlation between La_N/Sm_N and X_{Adr} and the lack of such a correlation between Gd_N/Yb_N and X_{Adr} (Fig. 7B, C), aligns with prediction from LST. This contrast further confirms that garnet compositional control is more important for LREE relative to HREE.

Garnet REE patterns

At the Lazhushan Fe skarn deposit, as the andradite content increases, the garnet REE patterns change from concave shapes (positive slopes of LREE and negative slopes of HREE) to negative shapes in chondrite-normalized REE diagrams (Fig. 4 A—D). Under equilibrium conditions, REE patterns of garnet are determined by garnet-fluid REE partition coefficients and fluid REE patterns. Using D_{La} as the reference value, the garnet (andradite-grossular)-fluid REE partition coefficient of a specific REE element (REEj) can be calculated via Eq. 11:

$$D_{REEj} = D_{La} \times \exp\{(-4\pi E_{M(3+)}N_A/RT) \times [r_{0(3+)}(r_{La}^2 - r_{REEj}^2)/2 - (r_{La}^3 - r_{REEj}^3)/3]\}, \quad (11)$$

where $r_{0(3+)}$ and $E_{M(3+)}$ are calculated via Eqs. 6 and 7, respectively. D_{La} is a constant under certain P, T, fluid chemistry and garnet composition conditions.

The D_{La} normalized values of garnet-fluid REE partition coefficients are illustrated in Fig. 8. As X_{Adr} increases, the shape of garnet-fluid REE partition coefficients changes from steep to shallow positive slope (Fig. 8 A, B). To demonstrate the impact of garnet composition on its REE patterns, we assume that the REE pattern of the diorite-derived fluid remains unchanged during garnet formation in the Lazhushan deposit. The REE composition of the diorite-derived fluid is modeled by using the average REE composition of endoskarn garnets (Sample LZS-11a) and the garnet-fluid REE coefficients at 600 °C, 0.1 GPa, and $X_{Adr} = 0.67$ (the average X_{Adr} of Sample LZS-11a). As shown in Fig. 8 D, the modeled fluid has a pattern characterized by strong LREE enrichment and HREE depletion, which is broadly comparable to the whole-rock REE patterns of diorite intrusions in the Daye district where the Lazhushan deposit is located (Li et al. 2009). The pattern of the modeled fluid is also similar to that of granitoid-derived fluid reported elsewhere (e.g., Banks et al. 1994).

The garnet REE patterns are modeled using the calculated garnet-fluid REE coefficients and fluid REE composition (Fig. 8C, D). As X_{Adr} increases from 0 to 1, the REE pattern of garnet gradually changes from HREE-enriched to LREE-enriched shape, with the latter resembling the REE pattern of the modeled fluid (Fig. 8C, D). This phenomenon is because REE fractionation is less effective in garnet with high X_{Adr} values (e.g., $X_{Adr} > 0.8$) (Fig.8 A, B), and fluid REE pattern (LREE-enriched) can overwhelm the influence of garnet-fluid REE partition coefficients. Garnets from the exoskarn sample (LZS-29) and the disseminated magnetite ore sample (LZS-5a) at Lazhushan have X_{Adr} values ranging from 0.47 to 0.66. These garnets

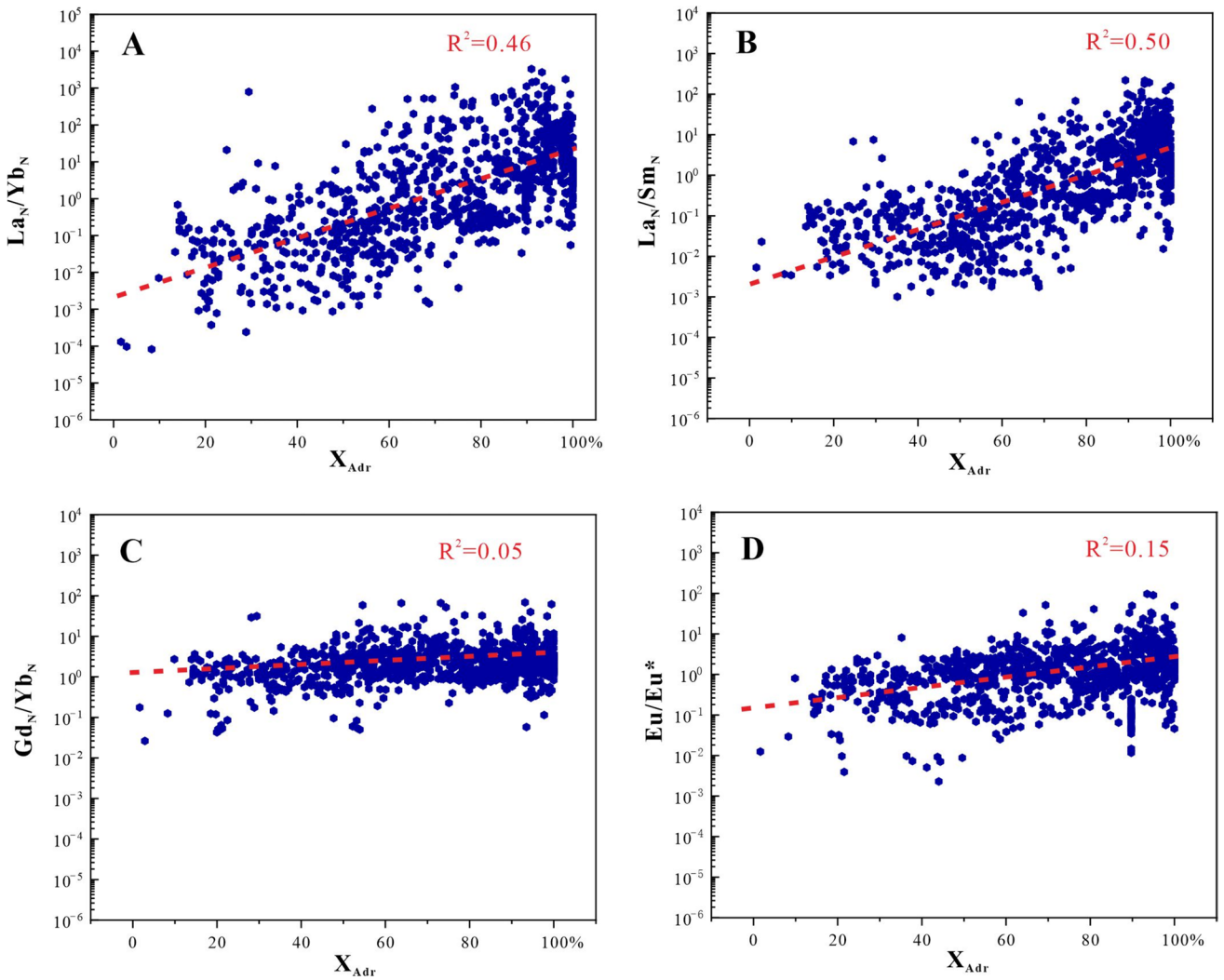

Fig. 7 X_{Adr} vs. La_N/Yb_N (**A**), La_N/Sm_N (**B**), Gd_N/Yb (**C**) and Eu/Eu^* (**D**) plots for garnets from skarn deposits worldwide

display positive slopes of LREE and flat to moderate negative slopes of HREE (Fig. 4B, C), which match the modeled garnet REE patterns in the same range of X_{Adr} (Fig. 9A, B). Garnets from the massive magnetite ore sample (LZS-32) have X_{Adr} values ranging from 0.84 to 0.96 and exhibit LREE-enriched and HREE-depleted patterns (Fig. 4D), broadly consistent with the modeled REE patterns of garnet in the same compositional range (Fig. 9C, D). Although grossular-rich garnets (e.g., $X_{Grs} > 0.8$) were not recognized in this study, they, if present, would likely display HREE-enriched patterns (Fig. 8C, D). Overall, the variations in REE patterns of garnet from the Lazhushan skarn deposit can be largely attributed to changing garnet major element composition.

The REE patterns of garnet from 22 skarn deposits worldwide are shown in Fig. 10. As garnet composition changes from grossularitic to andraditic, the REE patterns of garnet vary from positive through concave to negative shapes (Fig. 10). This is consistent with the trend observed in the Lazhushan deposit, confirming the significant role of garnet crystal chemistry in shaping garnet REE patterns.

The shift in REE patterns, transitioning from HREE-enriched to LREE-enriched shapes, has previously been interpreted as indicative of a transition from equilibrium to kinetic growth of skarn garnet (e.g., Park et al. 2017). REE patterns controlled by the kinetic effect (such as surface sorption) would only be preserved when the rate of mineral growth exceeds the rate of diffusive re-equilibration in the surface layer (McIntire 1963; Smith et al. 2004). Although oscillatory zonation, frequently observed in skarn garnets, is suggestive of such rapid growth, it is not conclusive evidence. In fact, garnets in sample LZS-5a exhibit oscillatory-zoned rims with REE patterns similar to those of the homogeneous core in the same garnet grain (Fig. 4C). The oscillatory zonation in our garnet likely resulted from periodic fluid flux derived from magmas. As demonstrated

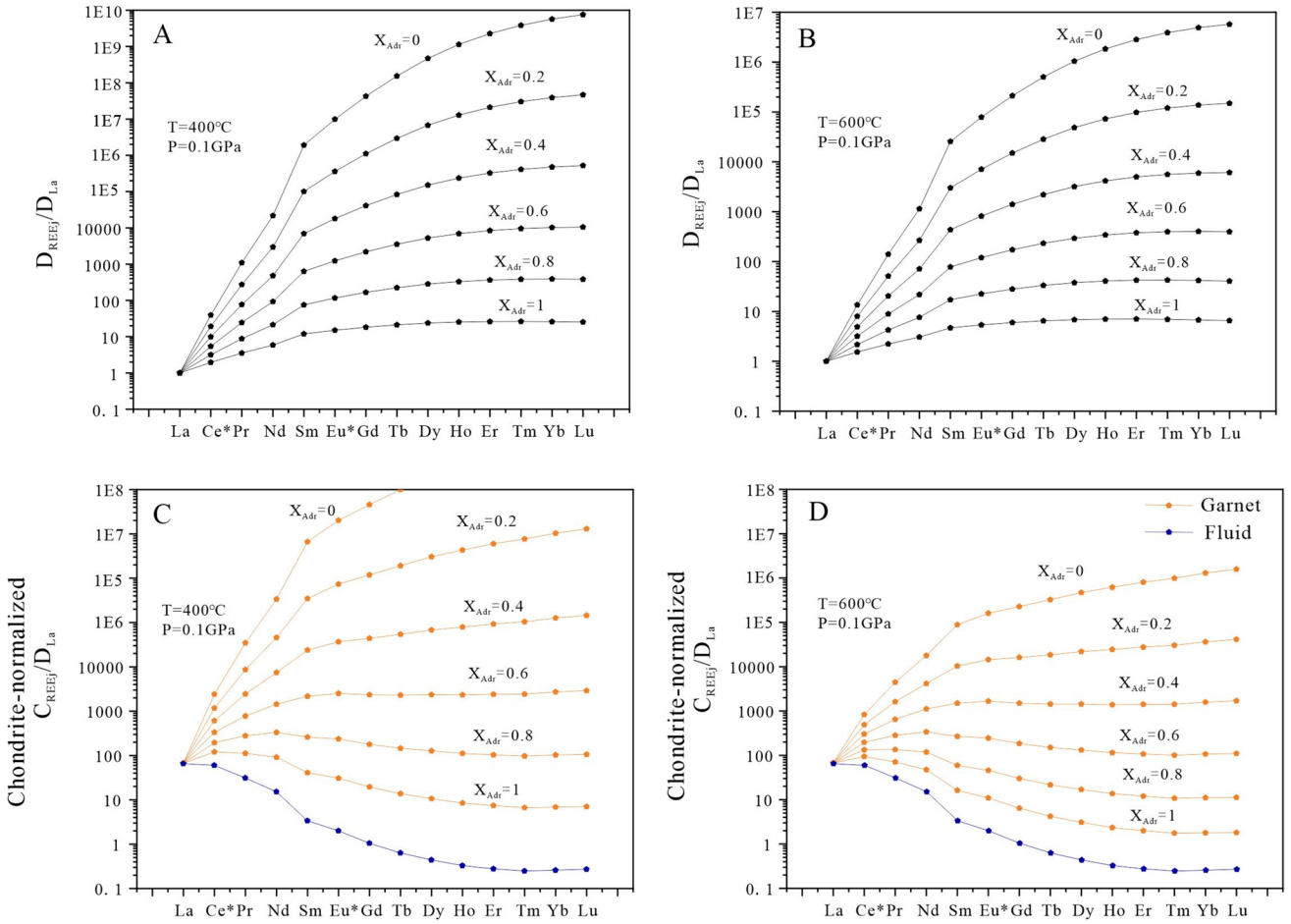

Fig. 8 The D_{La} normalized values of garnet-fluid REE coefficients at 400°C and 0.1 GPa (**A**) and 600°C and 0.1 GPa (**B**). The modeled garnet REE pattern at 400°C and 0.1 GPa (**C**). The modeled REE pattern of garnet and fluid at 600°C and 0.1 GPa (**D**). Note that Ce and Eu each has two valence states under natural conditions (Ce^{4+} and Ce^{3+}; Eu^{2+} and Eu^{3+}) and the LST equations used in here only constrain the garnet-fluid partition coefficients of Ce^{3+} and Eu^{3+}. The eightfold effective ionic radius of REE^{3+} from Shannon (1976)

earlier, the change in REE patterns can be readily explained by an increase in andradite content in garnets that have reached equilibrium with LREE-enriched fluids (Fig. 8). This aligns with the general assumption of local mineral-fluid equilibrium, or its near-attainment, in skarn formation processes (e.g., Reed 1997).

Garnet Eu anomaly

In chondrite-normalized diagrams, skarn garnets often exhibit a decoupling of Eu from its neighboring REE, Sm, and Gd (Figs. 4D, 10). Unlike Sm and Gd, which have a single valence state (Sm^{3+} and Gd^{3+}) in natural fluids, Eu exists in two valence states (Eu^{2+} and Eu^{3+}). The degree of Eu enrichment or depletion in garnet is quantified by the Eu anomaly, expressed as:

$$Eu/Eu^{*}_{Grt} = Eu_{Grt-N}/\mathrm{sqrt}\left(Sm_{Grt-N} \times Gd_{Grt-N}\right), \quad (12)$$

where Eu/Eu^{*}_{Grt} is garnet Eu anomaly and the subscript $_{Grt\text{-}N}$ designates chondrite-normalized concentration in garnet. $Eu_{Grt\text{-}N}$, $Sm_{Grt\text{-}N}$ and $Gd_{Grt\text{-}N}$ can be calculated as follows:

$$Eu_{Grt-N} = Eu_{fluid-N} \times D(Eu), \quad (13)$$

$$Sm_{Grt-N} = Sm_{fluid-N} \times D\left(Sm^{3+}\right), \quad (14)$$

$$Gd_{Grt-N} = Gd_{fluid-N} \times D\left(Gd^{3+}\right), \quad (15)$$

Here, D donates to garnet-fluid partition coefficient and the subscript $_{fluid\text{-}N}$ designates chondrite-normalized concentration in fluid coexisting with garnet. By introducing separate partition coefficients for Eu^{2+} and Eu^{3+}, the bulk garnet-fluid partition coefficient for Eu can be calculated as:

$$D(Eu) = f \times D\left(Eu^{2+}\right) + (1-f) \times D\left(Eu^{3+}\right), \quad (16)$$

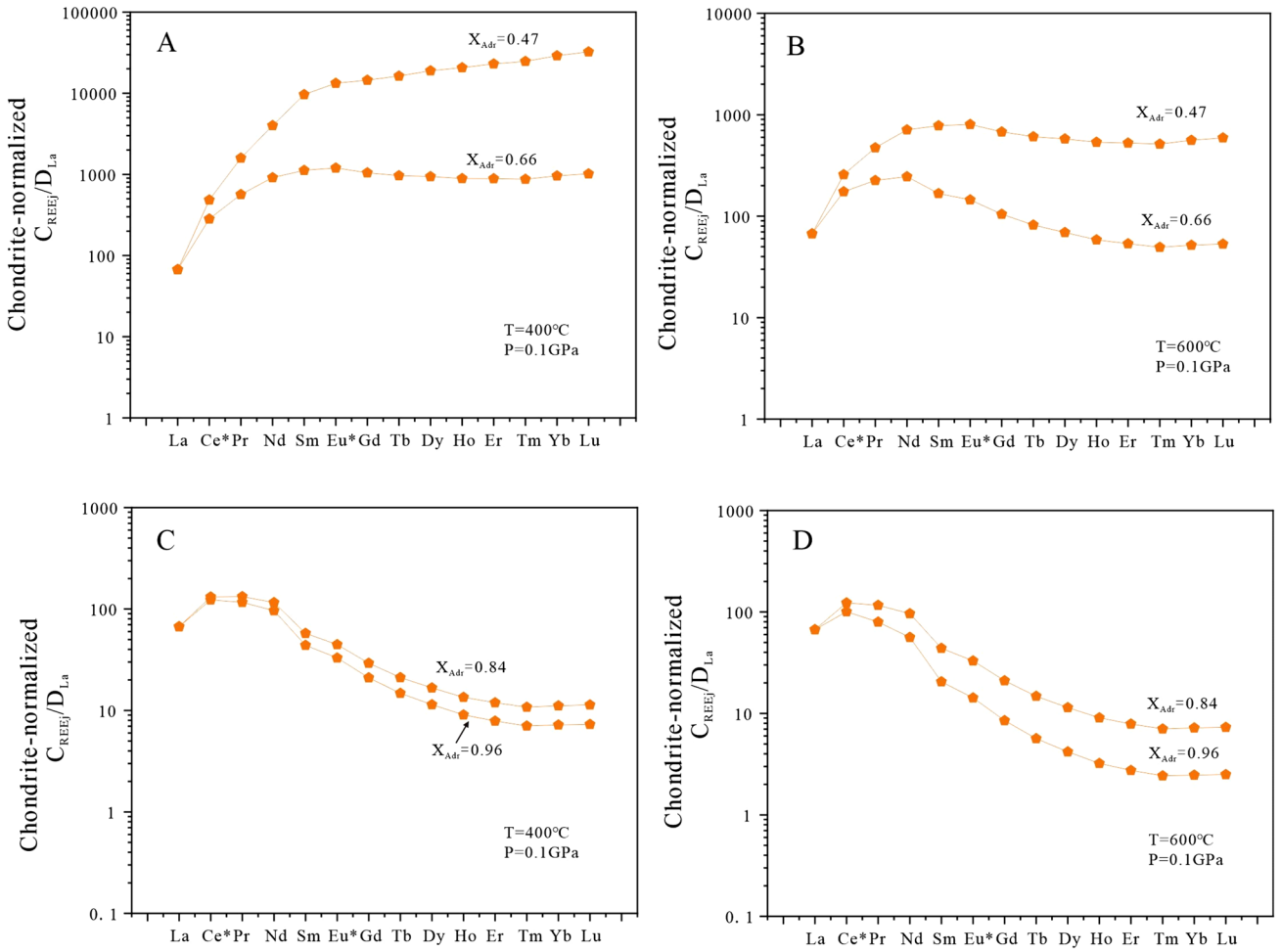

Fig. 9 The modeled REE pattern for the garnets from the exoskarn sample (LZS-29) and disseminated magnetite ore sample (LZS-5a) at 400°C and 0.1 GPa (**A**) and 600°C and 0.1 GPa (**B**). The modeled REE pattern for the garnets from the massive magnetite ore sample (LZS-5a) at 400°C and 0.1 GPa (**C**) and 600°C and 0.1 GPa (**D**)

where f is the fraction of Eu^{2+} to total Eu in fluid ($f = Eu^{2+}_{fluid\text{-}N}/Eu_{fluid\text{-}N}$, $0 < f < 1$). Considering fluid Eu anomaly:

$$Eu/Eu*_{fluid} = Eu_{fluid-N}/sqrt\,(Sm_{fluid-N} \times Gd_{fluid-N}), \quad (17)$$

Equations 12–17 can be combined to give:

$$Eu/Eu*Grt = Eu/Eu*fluid \times \left\{ f \times \frac{D(Eu2+)}{sqrt[D(Sm3+) \times D(Gd3+)]} + (1-f) \times \frac{D(Eu3+)}{sqrt[D(Sm3+) \times D(Gd3+)]} \right\}, \quad (18)$$

At 400 to 600 °C, 0.1GPa, $D(Eu^{3+})$ multiplied by the square root of $D(Sm^{3+}) \times D(Gd^{3+})$ closely approximates 1 (within a range of 1.01 to 1.09) for grossular-andradite garnet (Fig. 11A). To simplify, we use $D(Eu^{3+})$ to replace $sqrt[D(Sm^{3+}) \times D(Gd^{3+})]$ and this substitution, introducing an error less than 9% for the calculating of $Eu/Eu*_{Grt}$. Thus, Eq. 18 can be reduced to:

$$Eu/Eu*_{Grt} = Eu/Eu*_{fluid} \times \{f \times [D(Eu^{2+})/D(Eu^{3+}) - 1] + 1\}, \quad (19)$$

Theoretical predictions from Sverjensky (1984) showed an increase in the stability of Eu^{2+} over Eu^{3+} with increasing temperature and suggested that the Eu^{2+} is prevalent oxidation state for Eu in most crustal fluids at temperatures exceeding 250 °C. A study by Liu et al. (2016) using X-ray Absorption Spectroscopy (XAS) corroborates Sverjensky's predictions, demonstrating that even under relatively oxidizing conditions (involving a hematite-magnetite-pyrite assemblage) and at pH levels buffered by K-feldspar-muscovite-quartz, the fraction of divalent Eu to total Eu (referred to as "f") remains above 0.9 at 250 °C. Skarn garnets typically form at temperatures well above 250 °C, in chloride-rich and less oxidized fluids (e.g., Smith et al. 2004; Meinert et al. 2005; Gasper et al. 2008; Xu et al. 2020). This often leads

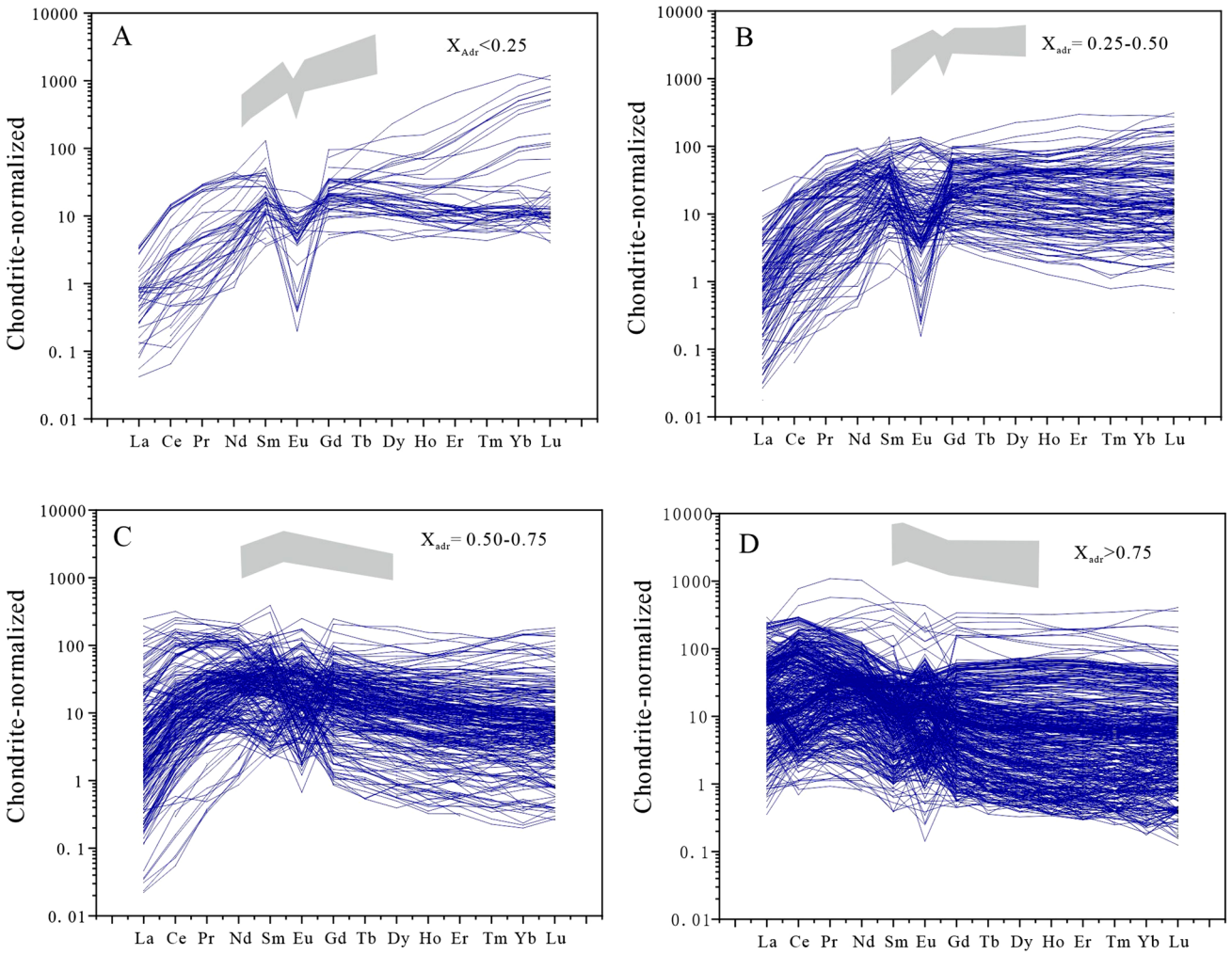

Fig. 10 The Chondrite-normalized REE patterns for garnets from 22 skarn deposits worldwide. Skarn garnets with low andradite contents ($X_{Adr}<0.25$) mostly display positive REE shapes with negative Eu anomalies (**A**); Skarn garnets with intermediate andradite contents ($0.25<X_{Adr}<0.75$) commonly display concave REE shapes (**B–C**). Skarn garnets with high andradite contents ($0.75<X_{Adr}$) generally display negative REE shapes (**D**). The grey lines represent the overall REE shapes of the given X_{Adr} range. Garnet REE patterns with zigzag segments and unrealistic anomalies (e.g., strong Tm positive/negative) that may represent incorrect analyses were removed from the figures

to "f" approaching unity for garnet-forming fluids. When "f" is sufficiently close to unity, Eq. 19 can be simplified as:

$$\mathrm{Eu/Eu}*_{\mathrm{Grt}} = \mathrm{Eu/Eu}*_{\mathrm{fluid}} \times [D(\mathrm{Eu}^{2+})/D(\mathrm{Eu}^{3+})], \quad (20)$$

According to Eq. 20, garnet Eu anomaly is a function of fluid Eu anomaly and $D(Eu^{2+})/D(Eu^{3+})$, the latter of which can be calculated using the following equation:

(Shannon 1976); $r_{0(3+)}$ and $E_{M(3+)}$ are calculated via Eqs. 6 and 7, respectively. The parameter of $D_{0(2+)}/D_{0(3+)}$ needed in calculating $D(Eu^{2+})/D(Eu^{3+})$ is largely unknown due to the absence of experimental data for garnet-fluid partitioning. This parameter is likely influenced by fluid chemistry due to differences in substitution mechanisms (e.g., $Ca^{2+} \longleftrightarrow Eu^{2+}$ verse $2Ca^{2+} \longleftrightarrow Eu^{3+} + Na^{+}$) and speciation effects between divalent

$$D(\mathrm{Eu}^{2+})/D(\mathrm{Eu}^{3+}) = \frac{D_0(2+) * \exp\{(-4\pi E_{M(2+)}N_A/RT) * [r_{0(2+)}(r_{Eu2} + -r_{0(2+)})^2/2 + (r_{Eu2} + -r_{0(2+)})^3/3]\}}{D_0(3+) * \exp\{(-4\pi E_{M(3+)}N_A/RT) * [r_{0(3+)}(r_{Eu3} + -r_{0(3+)})^2/2 + (r_{Eu2} + -r_{0(3+)})^3/3]\}}, \quad (21)$$

where $r_{0(2+)} = r_{0(3+)} + 0.04$ Å and $E_{M(2+)} = 2/3\ E_{M(3+)}$ (van Westrenen et al. 2001); $r_{Eu2+} = 1.25$ Å and $r_{Eu3+} = 1.066$ Å and trivalent cations (Brugger et al. 2000; 2008; Smith et al. 2004; van Hinsberg et al. 2010). Therefore, absolute values of

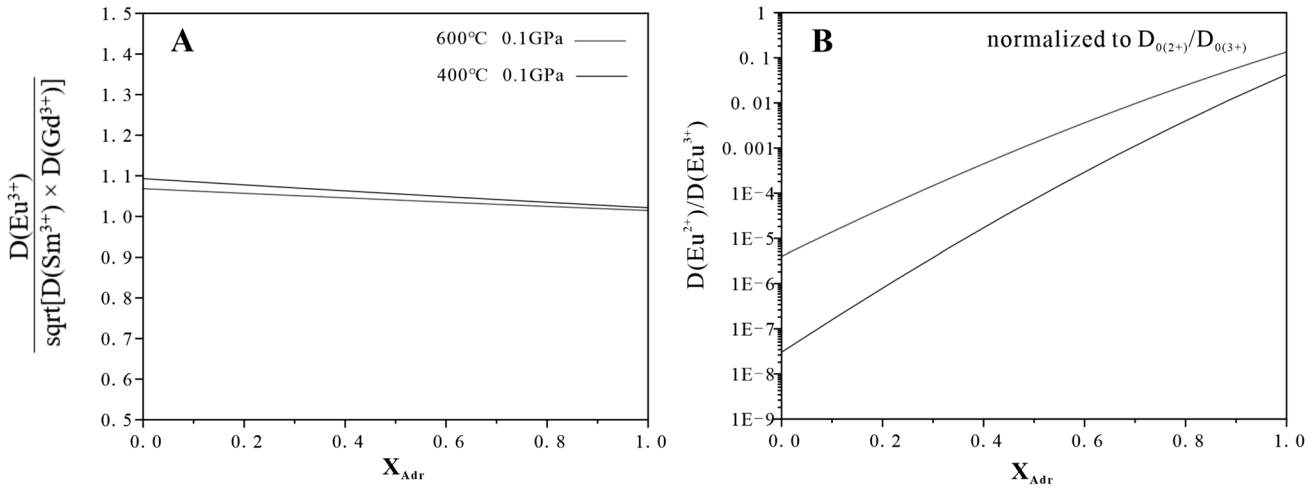

Fig. 11 X_{Adr} vs. $D(Eu^{3+})/sqrt[D(Sm^{3+})\times D(Gd^{3+})]$ (**A**) and $D_{0(2+)}/D_{0(3+)}$ normalized $D(Eu^{2+})/D(Eu^{3+})$ (**B**) plots. The ratio of $D(Eu^{3+})/sqrt[D(Sm^{3+})\times D(Gd^{3+})]$ is independent on D_0 and is calculated with $r_{0(3+)}$ and $E_{M(3+)}$ derived from Eqs. 6 and 7, respectively, and eightfold effective ionic radius of Eu^{3+}, Sm^{3+} and Gd^{3+} from Shannon (1976)

$D(Eu^{2+})/D(Eu^{3+})$ cannot be determined in this study. Nevertheless, when normalized to $D_{0(2+)}/D_{0(3+)}$, the apparent values of $D(Eu^{2+})/D(Eu^{3+})$ is very low for grossular-rich garnet but increases significantly with increasing X_{Adr} and temperature (Fig. 11B). This may explain the commonly observed negative Eu anomalies in grossular-rich garnet (Fig. 10A, B) and also the general positive correlation between garnet Eu anomaly and X_{adr} for skarn garnets in the global dataset (Fig. 7D). Note that, the correlation coefficient ($R^2=0.15$) is relatively modest for the garnets in the dataset (Fig. 7D), and a negative correlation is observed for garnets in the Lazhushan deposits (mainly caused by Sample LZS-32; Fig. 5D). This suggests that aside from garnet composition, other factors such as fluid Eu anomaly, fluid chemistry and temperature play important roles in controlling garnet Eu anomaly. As indicated by closed-system fractionation modeling, fluid Eu anomaly can vary by several orders of magnitude via precipitating reasonable amounts of scheelite and garnet itself (Brugger et al. 2000; Smith et al. 2004; Xu et al. 2020). Such variation in fluid Eu anomaly would translates into variation in garnet Eu anomaly if $D(Eu^{2+})/D(Eu^{3+})$ remains relatively constant (Eq. 20).

Implications

This study has substantial implications for understanding the REE systematics of skarn garnet. Previous studies have established that variations in the REE–pattern of skarn garnet are primarily associated with changing physiochemical parameters such as temperature, pH, and fluid chemistry as well as mineral growth rate (e.g., Jamtveit and Hervig 1994; Smith et al. 2004; Gasper et al. 2008; Zhai et al. 2014; Xu et al. 2020). These relationships have been widely used to elucidate the origin and evolution of both garnet and skarn-forming fluids (e.g., Park et al. 2017; Zhao et al. 2021; Huang et al. 2022; Ruan et al. 2022; Ghosh and Upadhyay 2022). In this study, we demonstrate a strong dependence of garnet REE patterns on garnet major element composition. Considering the strong correlation between the garnet major element composition and REE fractionations (Figs. 5, 7) and the fact that the garnet composition can change substantially within the scale of the deposit (from grossularitic to andraditic; e.g., Chang and Meinert 2008; Park et al. 2017), it becomes essential to carefully consider the influence of garnet crystal chemistry when interpreting garnet REE patterns.

Our study further illustrates that the LST equations allow for the prediction of fluid REE patterns based on garnet REE patterns, and vice versa. We demonstrate that the Eu anomaly in skarn garnet is mainly a function of fluid Eu anomaly and the garnet-fluid partition ratio of $D(Eu^{2+})/D(Eu^{3+})$. Garnet composition exerts controls on $D(Eu^{2+})/D(Eu^{3+})$ and consequently affects garnet Eu anomaly. These findings underscore the crucial role of garnet crystal chemistry in the REE fractionation of skarn garnets. Taking this factor into account can significantly enhance the reliability of using garnet REE as tracers in skarn systems.

Supplementary Information The online version contains supplementary material available at https://doi.org/10.1007/s00410-024-02095-3.

Acknowledgements This study was financially supported by the National Key Research and Development Program of China (No. 2023YFF0804200) and the National Natural Science Foundation of China (No. 42172101; No. 42321001; No. 41802114). We thank U.S. Geological Survey reviewer Dr. Ian W. Hillenbrand for review comments and suggestions. We thank Vincent van Hinsberg, Martin Smith and Lawrence Meinert for their constructive comments on early versions of the manuscript. Constructive reviews by Dr. Jan Kulhánek

and an anonymous reviewer significantly enhanced the quality of this manuscript. We express gratitude to Prof. Daniela Rubatto for her valuable comments and editorial handling. Any use of trade, firm, or product names is for descriptive purposes only and does not imply endorsement by the U.S. Government.

Data availability The authors confirm that the data supporting the findings of this study are availabe within the supplementatry materials.

Declarations

Conflict of interest The author declares that the submitted work does not bear any conflict of interest.

References

Aygül M, Okay AI, Hacker BR, Kylander-Clark ARC (2022) REE behavior in warm and cold subducting oceanic crust. Int J Earth Sci 111(3):905–918. https://doi.org/10.1007/s00531-021-02156-z

Banks DA, Yardley BWD, Campbell AR, Jarvis KE (1994) REE composition of an aqueous magmatic fluid: a fluid inclusion study from the Capitan Pluton, New Mexico, U.S.A. Chem Geol 113:259–272. https://doi.org/10.1016/0009-2541(94)90070-1

Blundy J, Wood B (1994) Prediction of crystal-melt partition coefficients from elastic moduli. Nature 372(6505):452. https://doi.org/10.1038/372452a0

Blundy J, Wood B (2003) Partitioning of trace elements between crystals and melts. Earth Planet Sci Lett 210(3):383–397. https://doi.org/10.1016/S0012-821X(03)00129-8

Brice JC (1975) Some thermodynamic aspects of the growth of strained crystals. J Cryst Growth 28(2):249–253. https://doi.org/10.1016/0022-0248(75)90241-9

Brugger J, Lahaye Y, Costa S, Lambert D, Bateman R (2000) Inhomogeneous distribution of REE in scheelite and dynamics of Archaean hydrothermal systems (Mt. Charlotte and Drysdale gold deposits, Western Australia). Contrib Mineral Petrol 139:251–264. https://doi.org/10.1007/s004100000135

Brugger J, Etschmann B, Pownceby M, Liu W, Grundler P, Brewe D (2008) Oxidation state of europium in scheelite: tracking fluid–rock interaction in gold deposits. Chem Geol 257(1):26–33. https://doi.org/10.1016/j.chemgeo.2008.08.003

Cahalan RC, Kelly ED, Carlson WD (2014) Rates of Li diffusion in garnet: coupled transport of Li and Y+REEs. Am Mineral 99(8–9):1676–1682. https://doi.org/10.2138/am.2014.4676

Carlson WD, Gale JD, Wright K (2014) Incorporation of Y and REEs in aluminosilicate garnet: energetics from atomistic simulation. Am Mineral 99(5–6):1022–1034. https://doi.org/10.2138/am.2014.4720

Chang Z, Meinert LD (2008) The empire Cu–Zn mine, idaho: exploration implications of unusual skarn features related to high fluorine activity. Econ Geol 103(5):909–938. https://doi.org/10.2113/gsecongeo.103.5.909

Chang Z, Shu Q, Meinert L (2019) Skarn deposits of China. In: Chang Z, Goldfarb RJ (eds) Mineral deposits of China, vol 22. Society of Economic Geologists Special Publication, pp 189–234. https://doi.org/10.12789/gs.v19i4.3773

Dana CDP, Agangi A, Idrus A, Chelle-Michou C, Lai C, Ishida M, Guillong M, González-Álvarez I, Takahashi R, Yano M, Mimura K, Ohta J, Kato Y, Simbolon DR, Xia X (2023) The age and origin of the ruwai polymetallic skarn deposit, Indonesia: evidence of cretaceous mineralization in the central borneo metallogenic belt. Econ Geol 118(6):1341–1370. https://doi.org/10.5382/econgeo.5009

Deer WAF, Howie RA, Zussman J (2013) An introduction to the rock-forming minerals. Mineralogical Society Great Britain Ireland. https://doi.org/10.1180/DHZ

Duan Z, Gleeson SA, Gao W-S, Wang F-Y, Li C-J, Li J-W (2020) Garnet U-Pb dating of the Yinan Au–Cu skarn deposit, Luxi district, North China craton: implications for district-wide coeval Au–Cu and Fe skarn mineralization. Ore Geol Rev 118:103310. https://doi.org/10.1016/j.oregeorev.2020.103310

Einaudi MT, Meinert LD, Newberry RJ (1981) Skarn deposits. Econ Geol. https://doi.org/10.5382/AV75.11

Fei X, Zhang Z, Cheng Z, Santosh M (2019) Factors controlling the crystal morphology and chemistry of garnet in skarn deposits: a case study from the cuihongshan polymetallic deposit, lesser Xing'an range. NE China Am Mineral 104(10):1455–1468. https://doi.org/10.2138/am-2019-6968

Gaspar M, Knaack C, Meinert LD, Moretti R (2008) REE in skarn systems: A LA-ICP-MS study of garnets from the crown jewel gold deposit. Geochim Cosmochim Acta 72(1):185–205. https://doi.org/10.1016/j.gca.2007.09.033

George FR, Gaidies F, Boucher B (2018) Population-wide garnet growth zoning revealed by LA-ICP-MS mapping: implications for trace element equilibration and syn-kinematic deformation during crystallisation. Contrib Mineral Petrol 173(9):74. https://doi.org/10.1007/s00410-018-1503-0

Ghosh U, Upadhyay D (2022) The retrograde evolution of F-rich skarns: clues from major and trace element chemistry of garnet, scheelite, and vesuvianite from the Belka Pahar wollastonite deposit. India Lithos 422–423:106750. https://doi.org/10.1016/j.lithos.2022.106750

Godet A, Raimondo T, Guilmette C (2022) Atoll garnet: insights from LA-ICP-MS trace element mapping. Contrib Mineral Petrol 177(6):57. https://doi.org/10.1007/s00410-022-01924-7

Goncalves P, Raimondo T, Paquette J, De Souza S, De Oliveira J (2021) Garnet as a monitor for melt–rock interaction: textural, mineralogical, and compositional evidence of partial melting and melt-driven metasomatism. J Metamorph Geol 39(5):617–648. https://doi.org/10.1111/jmg.12592

Harris NBW, Gravestock P, Inger S (1992) Ion-microprobe determinations of trace-element concentrations in garnets from anatectic assemblages. Chem Geol 100(1):41–49. https://doi.org/10.1016/0009-2541(92)90101-A

Huang X-D, Lu J-J, Zhang R-Q, Sizaret S, Ma D-S, Wang R-C, Zhu X, He Z-Y (2022) Garnet and scheelite chemistry of the Weijia tungsten deposit, South China: implications for fluid evolution and W skarn mineralization in F-rich ore system. Ore Geol Rev 142:104729. https://doi.org/10.1016/j.oregeorev.2022.104729

Irving AJ, Frey FA (1978) Distribution of trace elements between garnet megacrysts and host volcanic liquids of kimberlitic to rhyolitic composition. Geochim Cosmochim Acta 42(6):771–787. https://doi.org/10.1016/0016-7037(78)90092-3

Jamtveit B (1991) Oscillatory zonation patterns in hydrothermal grossular-andradite garnet; nonlinear dynamics in regions of immiscibility. Am Mineral 76(7–8):1319–1327. https://doi.org/10.1346/CCMN.1991.0390413

Jamtveit B, Hervig RL (1994) Constraints on transport and kinetics in hydrothermal systems from zoned garnet crystals. Science 263(5146):505. https://doi.org/10.1126/science.263.5146.505

Konrad-Schmolke M, Halama R, Chew D, Heuzé C, De Hoog J, Ditterova H (2023) Discrimination of thermodynamic and kinetic contributions to the heavy rare earth element patterns in metamorphic garnet. J Metamorph Geol 41(4):465–490. https://doi.org/10.1111/jmg.12703

Kulhánek J, Faryad SW (2023) Compositional changes in garnet: trace element transfer during eclogite-facies metamorphism.

Contrib Mineral Petrol 178(10):68. https://doi.org/10.1007/s00410-023-02050-8
Kulhánek J, Faryad SW, Jedlicka R, Svojtka M (2021) Dissolution and reprecipitation of garnet during eclogite-facies metamorphism; major and trace element transfer during atoll garnet formation. J Petrol 62(11):egab77. https://doi.org/10.1093/petrology/egab077
Li J-W, Zhao X-F, Zhou M-F, Ma C-Q, de Souza ZS, Vasconcelos P (2009) Late mesozoic magmatism from the daye region, eastern China: U-Pb ages, petrogenesis, and geodynamic implications. Contrib Mineral Petrol 157(3):383–409. https://doi.org/10.1007/s00410-008-0341-x
Liu Y, Hu Z, Gao S, Günther D, Xu J, Gao C, Chen H (2008) In situ analysis of major and trace elements of anhydrous minerals by LA-ICP-MS without applying an internal standard. Chem Geol 257(1):34–43. https://doi.org/10.1016/j.chemgeo.2008.08.004
Liu W, Etschmann B, Migdisov A, Boukhalfa H, Testemale D, Müller H, Hazemann J-L, Brugger J (2017) Revisiting the hydrothermal geochemistry of europium (II/III) in light of new in-situ XAS spectroscopy results. Chem Geol 459:61–74. https://doi.org/10.1016/j.chemgeo.2017.04.005
Liu L, Zhou T, Zhang D, Liu G, Zhao Z, Sun J, White NC (2021) Major and trace elements analyses of garnet from the Haobugao Zn-Fe-Sn polymetallic deposit, northeast China: implications for skarn formation and hydrothermal fluid evolution. Ore Geol Rev 138:104337. https://doi.org/10.1016/j.oregeorev.2021.104337
McDonough WF, Sun SS (1995) The composition of the Earth. Chem Geol 120(3):223–253. https://doi.org/10.1016/0009-2541(94)00140-4
McIntire WL (1963) Trace element partition coefficients—a review of theory and applications to geology. Geochim Cosmochim Acta 12:1209–1264
Meinert LD (1992) Skarns and skarn deposits. Geosci Can 19:145–162
Meinert LD, Dipple GM, Nicolescu S (2005) World skarn deposits. In: Hedenquist JW, Thompson JFH, Goldfarb RJ, Richards JP (eds) Economic geology, one hundredth anniversary. Society of Economic Geologists. https://doi.org/10.5382/AV100.11
Park C, Song Y, Kang I-M, Shim J, Chung D, Park C-S (2017) Metasomatic changes during periodic fluid flux recorded in grandite garnet from the Weondong W-skarn deposit, South Korea. Chem Geol 451:135–153. https://doi.org/10.1016/j.chemgeo.2017.01.011
Reed MN (1997) Hydrothermal alteration and its relationship to ore fluid composition. In: Barnes HL (ed) Geochemistry of hydrothermal ore deposits. Wiley, New York, pp 303–365
Ruan C-T, Yu X-Y, Su S-G, Santosh M, Qin L-J (2022) Anatomy of garnet from the nanminghe skarn iron deposit, China: implications for ore genesis. Minerals 12(7):845. https://doi.org/10.3390/min12070845
Rubatto D (2002) Zircon trace element geochemistry: partitioning with garnet and the link between U-Pb ages and metamorphism. Chem Geol 184(1):123–138. https://doi.org/10.1016/S0009-2541(01)00355-2
Rubatto D, Burger M, Lanari P, Hattendorf B, Schwarz G, Neff C, Keresztes Schmidt P, Hermann J, Vho A, Günther D (2020) Identification of growth mechanisms in metamorphic garnet by high-resolution trace element mapping with LA-ICP-TOFMS. Contrib Mineral Petrol 175(7):61. https://doi.org/10.1007/s00410-020-01700-5
Shannon RD (1976) Revised effective ionic radii and systematic studies of interatomic distances in halides and chalcogenides. Acta Crystallogr A 32(5):751–767. https://doi.org/10.1107/S0567739476001551
Sisson TW, Bacon CR (1992) Garnet/high-silica rhyolite trace element partition coefficients measured by ion microprobe. Geochim Cosmochim Acta 56(5):2133–2136. https://doi.org/10.1016/0016-7037(92)90336-H
Smith MP, Henderson P, Jeffries TER, Long J, Williams CT (2004) The rare earth elements and uranium in garnets from the beinn an dubhaich Aureole, Skye, Scotland, UK: constraints on processes in a dynamic hydrothermal system. J Petrol 45(3):457–484. https://doi.org/10.1093/petrology/egg087
Stalder R, Foley SF, Brey GP, Horn I (1998) Mineral-aqueous fluid partitioning of trace elements at 900–1200°C and 3.0–5.7 GPa: new experimental data for garnet clinopyroxene and rutile and implications for mantle metasomatism. Geochim Cosmochim Acta 62(10):1781–1801. https://doi.org/10.1016/S0016-7037(98)00101-X
Sverjensky DA (1984) Europium redox equilibria in aqueous solution. Earth Planet Sci Lett 67(1):70–78. https://doi.org/10.1016/0012-821X(84)90039-6
Van Hinsberg VJ, Migdisov AA, Williamsjones AE (2010) Reading the mineral record of fluid composition from element partitioning. Geology 38(9):847–850. https://doi.org/10.1130/G31112.1
van Hinsberg VJ, Berlo K, Pinti DL, Ghaleb B (2021) Gypsum Precipitating From Volcanic Effluent as an Archive of Volcanic Activity. Front Earth Sci. https://doi.org/10.3389/feart.2021.764087
van Westrenen W, Draper DS (2007) Quantifying garnet-melt trace element partitioning using lattice-strain theory: new crystal-chemical and thermodynamic constraints. Contrib Mineral Petrol 154(6):717–730. https://doi.org/10.1007/s00410-007-0222-8
van Westrenen W, Blundy J, Wood B (1999) Crystal-chemical controls on trace element partitioning between garnet and anhydrous silicate melt. Am Mineral 84(5–6):838–847. https://doi.org/10.2138/am-1999-5-617
van Westrenen W, Wood BJ, Blundy JD (2001) A predictive thermodynamic model of garnet–melt trace element partitioning. Contrib Mineral Petrol 142(2):219–234. https://doi.org/10.1007/s004100100285
Vho A, Daniela R, Pierre L, Francesco G, Daniele R, Jörg H (2020) Crustal reworking and hydration: insights from element zoning and oxygen isotopes of garnet in high-pressure rocks (Sesia Zone, Western Alps). Contrib Mineral Petrol 175(11):109. https://doi.org/10.1007/s00410-020-01745-6
Wang Y-C, Duan D-F (2021) REE Distribution character in skarn garnet and its geological implication. Acta Scientiarum Naturalium Universitatis Pekinensis 57:446–458. https://doi.org/10.13209/j.0479-8023.2021.006
Wen G, Li J-W, Hofstra AH, Koenig AE, Cui B-Z (2020) Textures and compositions of clinopyroxene in an Fe skarn with implications for ore-fluid evolution and mineral-fluid REE partitioning. Geochim Cosmochim Acta 290:104–123. https://doi.org/10.1016/j.gca.2020.08.020
Whitehouse MJ, Platt JP (2003) Dating high-grade metamorphism—constraints from rare-earth elements in zircon and garnet. Contrib Mineral Petrol 145(1):61–74. https://doi.org/10.1007/s00410-002-0432-z
Xiao X, Zhou T-F, White NC, Zhang L-J, Fan Y, Wang F-Y, Chen X-H (2018) The formation and trace elements of garnet in the skarn zone from the Xinqiao Cu-S-Fe-Au deposit, Tongling ore district, Anhui Province, Eastern China. Lithos 302–303:467–479. https://doi.org/10.1016/j.lithos.2018.01.023
Xu J, Ciobanu CL, Cook NJ, Zheng Y, Sun X, Wade BP (2016) Skarn formation and trace elements in garnet and associated minerals from zhibula copper deposit, gangdese Belt, southern Tibet. Lithos 262:213–231. https://doi.org/10.1016/j.lithos.2016.07.010
Xu J, Ciobanu CL, Cook NJ, Zheng Y, Li X, Wade BP, Verdugo-Ihl MR, Gao W, Zhu Q (2020) Numerical modelling of rare earth element fractionation trends in garnet: a tool to monitor skarn evolution. Contrib Mineral Petrol 175(4):30. https://doi.org/10.1007/s00410-020-1670-7

Zhai D-G, Liu J-J, Zhang H-Y, Wang J-P, Su L, Yang X-A, Wu S-H (2014) Origin of oscillatory zoned garnets from the Xieertala Fe–Zn skarn deposit, northern China: In situ LA–ICP-MS evidence. Lithos 190–191:279–291. https://doi.org/10.1016/j.lithos.2013.12.017

Zhang S, Chen H, Shu Q, Zhang Y, Chu G, Cheng J, Tian J (2019) Unveiling growth histories of multi-generational garnet in a single skarn deposit via newly-developed LA-ICP-MS U-Pb dating of grandite. Gondwana Res 73:65–76. https://doi.org/10.1016/j.gr.2019.04.003

Zhao WW, Zhou M-F, Williams-Jones AE, Zhao Z (2018) Constraints on the uptake of REE by scheelite in the Baoshan tungsten skarn deposit, South China. Chem Geol 477:123–136. https://doi.org/10.1016/j.chemgeo.2017.12.020

Zhao L, Zhang Y, Shao Y, Li H, Ahmad Shah S, Zhou W (2021) Using garnet geochemistry discriminating different skarn mineralization systems: perspective from huangshaping W-Mo-Sn-Cu polymetallic deposit. South China Ore Geol Rev 138:104412. https://doi.org/10.1016/j.oregeorev.2021.104412